Chemical Engineering Journal 467 (2023) 143239

Contents lists available at ScienceDirect

Chemical Engineering Journal

journal homepage: www.elsevier.com/locate/cej

Adjustment of the ZSM-5 zeolite support towards the efficient hydrogen production by ethanol steam reforming on cobalt catalysts

Gabriela Grzybek [a,*], Magdalena Greluk [b], Piotr Patulski [a], Paweł Stelmachowski [a], Karolina Tarach [a], Grzegorz Słowik [b], Marek Rotko [b], Susana Valencia [c], Fernando Rey [c], Kinga Góra-Marek [a]

[a] Faculty of Chemistry, Jagiellonian University in Kraków, Gronostajowa 2, 30-387 Krakow, Poland
[b] Faculty of Chemistry, Maria Curie-Sklodowska University in Lublin, Maria Curie-Sklodowska Sq. 3, 20-031 Lublin, Poland
[c] Instituto de Tecnologia Quimica (Universitat Politecnica de Valencia – Consejo Superior de Investigaciones Cientificas), Avda. de Los Naranjos s/n, Valencia 46022, Spain

ARTICLE INFO

Keywords:
Cobalt catalyst
ZSM-5 zeolite
Ethanol steam reforming
Hydrogen production
Acidity
Silicalite

ABSTRACT

The world is on track for replacing fossil fuels with alternative energy carriers. In the face of the ongoing global energy transformation, the focus is on hydrogen. Its production in the ethanol steam reforming (ESR) process with the use of a substrate from bio-sources deserves special attention. The ESR process requires a catalyst, which should be selective and resistant to the deactivation processes. We have taken a challenge to develop the cobalt catalyst based on the ZSM-5 zeolite support. We synthesized a series of catalysts based on zeolite with increasing Si/Al ratios (32, 750, ∞ that is Al-free zeolite) and different zeolite morphology. The substantial difference in their performance we discussed based on the multifaceted physicochemical characterization and unique *operando* UV–Vis and FT-IR spectroscopy studies in the ESR conditions. We have checked the effect of potassium introduction to the Co|ZSM-5 catalyst. The increase in ethanol conversion and decrease in selectivity to undesired C2H4 product with the decrease of the Al content, and further competitive activity and stability of the Al-free catalyst we discussed in terms of the zeolite acidity and its impact on the cobalt phase oxidation state. The advantage of nanometric zeolite over the micrometric one, we attributed to much better dispersion of cobalt active phase over its surface. Thus, the adjustment of zeolite support properties allows us to get the extraordinary ESR catalyst. Our results overthrow the existing paradigm of low activity and stability of zeolite-based ESR catalysts, opening the way to the development of competitive catalysts that give real hope for implementation.

1. Introduction

The well-defined porous structure, large surface area, and ion-exchange properties make zeolites objects of interest in many fields. They are utilized, e.g., as molecular sieves for separating molecules according to their dimensions, as adsorbents for water, soil, and air purification, for removing radioactive contaminants, as detergents, as catalysts support, and as catalysts themselves e.g., in the petrochemical industry [1–3]. In addition, to use in traditional petrochemical industries, zeolites are also intensively studied for other sustainable catalytic processes, including air pollution abatement (i.e. NO_x removal), CO_2 capture and conversion, and biomass conversion [4–6]. Also, research on the ethanol steam reforming (ESR) process on zeolite-based catalysts is in progress [7]. The authors reported the use of Y [8–12], BEA (beta) [13–17], MOR (mordenite) [18], ITQ-2 [19], and ITQ-18 [20] zeolites modified with metallic active phases, such as copper [14,16], cobalt [8,10,19,20], nickel [9,13–15,17–19], and rhodium [12] in the ESR process. ZSM-5 zeolite was also considered as a support for the ESR cobalt catalyst [8,21–23]. The available reports focused on zeolite structures containing a significant number of aluminium atoms (Al). In each of the reports, the Al content in the zeolites was in the range of Si/Al = 25–35 for cobalt catalysts and Si/Al = 20–80 for catalysts containing other active metals, such as Cu, Ni, and Rh, or Pd.

Nevertheless, the share of papers on ethanol steam reforming on zeolite-supported catalysts is minor compared to those dedicated to materials based on metal oxide supports such as cerium oxide, zirconia oxide, alumina, magnesium oxides, silica, and mixed oxides e.g. cerium alumina [24–33]. The authors in the review papers [32,34–36]

* Corresponding author.
E-mail address: g.grzybek@uj.edu.pl (G. Grzybek).

https://doi.org/10.1016/j.cej.2023.143239
Received 14 February 2023; Received in revised form 25 March 2023; Accepted 26 April 2023
Available online 9 May 2023

concerning the ethanol steam reforming process summarized several dozen of laboratory-scale research of noble Rh, Pt, Ru, and Ir-based as well as non-noble Co, Ni, Cu, and Mn-based metal oxide supported catalysts. From this wide group, the ceria supported cobalt catalysts are very promising materials due to active surface oxygen in CeO_2 which stimulates coke removal ability. Recently Li et al. in [37] has shown that catalyst performance can be successfully improved by upon tuning the chemical state of cobalt phase by preferred exposure of ceria facets. The oxidation state of the cobalt phase is important for both ethanol conversion and coking suppression. If both metallic Co^0 and Co^{2+} species are present, a catalyst is active, stable, and resistant for coking. Co^0 species promote C–C bond scission, while Co^{2+} species activate water [32].

As underlined in [32], the minor interest in zeolites for the application for ESR results from their high density of acid sites, which results in a significant contribution to the undesired path of ethanol dehydration towards C_2H_4 followed by a significant amount of carbon deposit and hence deactivation of the catalyst. However, the outstanding textural properties make zeolites notable candidates for the development of competitive ESR catalysts.

The effectivity of zeolite-based catalysts in the ESR process can be enhanced by eliminating the acidic properties of zeolite by using two main strategies, namely alkali doping and the decrease of the Si/Al ratio in the zeolite support. Indeed, most of the zeolite-based catalysts studied for the ESR process are alkali-exchanged ones. The sodium, cesium, and potassium forms of zeolite Y and ZSM-5 were reported [7,12,38,39]. It has to be underlined that these reports relate to activity tests lasting only 5–6 h, in which the sodium, cesium, and potassium forms of the catalysts show stable activity and selectivity. However, these reports do not show catalytic data for long-term reactions that would indicate their stability over time, e.g., 100 h of the ESR process, which seems to be crucial taking into account the high mobility of alkali admixtures [40]. In terms of the Al removal approach, even though the zeolites with a wide Al content range were investigated, systematic studies showing the direct relationship between Si/Al and catalytic performance in the ESR process have not been reported yet.

In this paper, we focus on the adjustment of the medium-pore ZSM-5 zeolite support properties defined by its acidity and its crystal morphology towards the efficient hydrogen production by ethanol steam reforming on cobalt catalysts. We prepared a series of cobalt catalysts supported on ZSM-5 zeolite that varies in Al content (Si/Al 32, 750, Al-free). Referring to the crystal morphology of the zeolite, we prepared the reference catalyst supported on the pure siliceous supports, that is, amorphous SiO_2 and ZSM-5 of various crystal sizes. The multifaceted physicochemical characterization of fresh and spent catalysts using FT-IR pyridine and CO sorption studies, temperature-programmed reduction studies (H_2-TPR), high-resolution transmission electron microscopy with energy-dispersive X-ray spectroscopy (HR-TEM/EDX), *in situ* X-ray photoelectron spectroscopy (XPS), Raman spectroscopy (RS), and thermogravimetric analysis (TGA) was performed to obtain a comprehensive picture of the factors influencing the catalyst activity and selectivity. The stability of the catalysts was tested in short (21 h) and long-term (>160 h) catalytic experiments. In addition, the *operando* UV–vis and FT-IR studies of Co reduction, and ESR processes were performed. We accounted for the great variation in catalyst performance in the ESR process by the differences in the catalyst acidity, reducibility, and morphology of the zeolite support crystals. In addition, we hypothesized a synergic effect of potassium doping and the limited presence of aluminium atoms (Lewis acid sites) in the commercially available carrier Z(750) and we checked the effect of potassium addition on the catalytic performance of the Co|Z(750) catalyst.

2. Experimental

2.1. Supports

Zeolite ZSM-5 (donated as Z in sample names) with Si/Al = 32 (CBV 5524G, ZEOLYST) hereafter denoted Z(32), high-silica zeolite ZSM-5 with Si/Al = 750 (HSZ-890HOA, TOSOH Corporation) hereafter denoted Z(750) as well as reference silica (Aerosil 200, Evonik Industries AG) hereafter denoted SiO_2(ref) come from commercial sources.

We also prepared pure silica ZSM-5 counterparts to follow the influence of support's acidity. Further, the morphology influence on the ESR performance was checked with two purely siliceous ZSM-5 counterparts. Purely siliceous ZSM-5 zeolite supports, differing in crystal size, *Z(∞)-B and Z(∞)-S,* were synthesized according to the procedures as follows. Synthesis of pure silica ZSM-5 of micrometric size grains labeled Z(∞)-B, was performed according to the verified procedure described elsewhere [41]. The synthesis was done with the use of tetrapropylammonium bromide (TPABr, Aldrich, 98%) as a structure-directing agent (SDA). Aerosil 200 was used as a silica source. The final gel composition was $1SiO_2$:0.08SDA:NH_4F:$20H_2O$. Aerosil 200 was stirred mechanically with an aqueous solution of TPABr and NH_4F (Aldrich) for 30 min. The dense gel obtained was transferred into Teflon-lined stainless steel autoclaves and heated to 175 °C in static conditions, the synthesis was performed for 4 days. The material obtained was washed and dried at 100 °C. Total calcination of the final sample was done at 700 °C for 8 h, with a rate of 1 °C·min^{-1}. The synthesis of nanometric pure silica ZSM-5 zeolite of the significantly reduced size of crystals labeled Z(∞)-S, was carried out using the tetrapropylammonium hydroxide (TPAOH, Aldrich, 40% in water) as SDA [42]. The gel composition for the synthesis of zeolite was SiO_2:0.25SDA:9.7EtOH:$24H_2O$. The applied silica source was tetraethylorthosilicate (TEOS, Merck, >98%). The appropriate amount of TEOS was hydrolysed in an aqueous solution of SDA and ethanol (EtOH, Aldrich, absolute). The mixture obtained was stirred mechanically at room temperature for 2 h. The gel was then transferred to Teflon-lined stainless steel autoclaves where the synthesis was performed under constant rotation of the autoclaves at 150 °C for 14 days. The sample was calcined at 550 °C for 6 h, with a rate of 2 °C·min^{-1}.

2.2. Cobalt catalysts preparation

The cobalt active phase (10 wt%) was deposited on the zeolite supports and reference SiO_2 using the incipient wetness impregnation (IWI) method from an aqueous solution of cobalt nitrate hexahydrate (Aldrich, 98%), the resulting samples were labeled as Co|Z(32), Co|Z(750), Co|Z(∞)-S, Co|Z(∞)-B, and Co|SiO_2(ref). Potassium was introduced in the amount of 2 wt% onto the surface of the Co|Z(750) catalyst by the IWI method, using an aqueous solution of potassium nitrate (Aldrich, 98%) with the appropriate concentration, the sample was labeled Co|ZSM(750)-IWI. Additionally, the K-exchanged sample was prepared by the ion-exchange (IE) of zeolite support using an aqueous solution of KNO_3 (Aldrich, 98%). The suspension obtained was stirred at 80 °C with a magnetic stirrer for 6 h and then filtered and dried. The potassium-exchanged zeolite was then loaded with the cobalt phase by the IWI method, and the resulting sample was labeled Co|ZSM(750)-IE. All final materials were dried at RT for 24 h followed by calcined at 500 °C for 2 h at a rate of 1 °C/min.

2.3. Characterization methods

The silica-to-aluminium molar ratio of the supports was analyzed with a PerkinElmer Optima 2100DV ICP-OES spectrometer. The cobalt phase content was verified employing the XRF spectrometer (ARL QUANT'X). The Rh anode was applied to generate the X-rays of 4–50 kV (1 kV step). The 3.5 mm Si(Li) drifted crystal with the Peltier cooling (~185 K) was applied as a de- tector. The UniQuant software was used

for the evaluation of the registered data. The specific surface area and porosity of the supports and as-prepared cobalt catalysts were analyzed by N_2-physisorption at −196 °C using a Quantachrome Autosorb- 1-MP gas sorption instrument according to the procedure described elsewhere [8]. The results of this textural characterization are presented in Table S1. Powder XRD patterns for supports and prepared cobalt catalysts were recorded using a Rigaku Multiflex diffractometer, using Cu Kα radiation (40 kV, 40 mA). The diffractograms were recorded in the 2θ angle range of 10–50° with a step size of 0.02° and an accumulation time of 3 s. The reducibility of the prepared materials was investigated with the AutoChem II 2920 instrument (Micromeritics, USA). Details of the TPR measurements are detailed in [10].

The acidic properties of the reduced catalysts were investigated in quantitative FT-IR experiments of pyridine (Py) and carbon monoxide sorption to probe the Brønsted and Lewis acid sites, and the cobalt sites, respectively. The samples were pressed to the form of a disc and then placed in a custom-made quartz IR cell. *In situ* evacuation at 500 °C under vacuum (10^{-5} mbar) for 1 h was followed by treatment in a pure hydrogen atmosphere at 550 °C for 1 h and cooling down to the temperature required for Py or CO sorption experiments. The neutralization of all acid sites was realized by saturation of the samples with the Py vapors at 170 °C under static conditions. Then, gaseous and physisorbed Py molecules were removed by desorption at 170 °C and the spectra were collected. These spectra served to determine the intensities of the Py bands at 1545 cm^{-1} (pyridinium ions, PyH^+) and 1455–1442 cm^{-1} (Py coordinatively bonded to Lewis sites, PyL). The latter values, determined for each band after deconvolution if necessary, together with the respective absorption coefficients: 0.07 $cm^2 \cdot \mu mol^{-1}$ for the 1545 cm^{-1} band of PyH^+ and 0.10 $cm^2 \cdot \mu mol^{-1}$ for the 1455–1442 cm^{-1} band of PyL, were used to calculate the concentration of Brønsted and Lewis acid sites. The low-temperature sorption (−100 °C) of carbon monoxide (CO, Linde Gas Poland, 99.95%) allowed us to distinguish between the oxo-species and cation-exchanged cobalt species [10]. All spectra presented in this work were recorded by gathering 500 scans with a spectral resolution of 2 cm^{-1} on a Vertex 70 spectrometer (Bruker) equipped with an MCT detector. Based on the methodology of quantitative measurement developed for cobalt sites in zeolites [43], the concentrations of isolated cobalt ions and cobalt ions in oxide forms were determined.

Micrographs of studied pure silica zeolites were obtained with the use of FE-SEM (Field Emission Scanning Electron Microscope, Zeiss, Ultra 55). For analysis purposes, the samples were deposited on double-sided tape and analyzed without a metal covering.

The morphology and elemental repartition of the reduced and spent catalysts were studied with the high-resolution transmission electron microscope (HR-TEM, Titan G2 60–300 kV, FEI Company), equipped with energy-dispersive X-ray spectroscopy (EDX). Phase separation in the samples was performed with a fast Fourier transformation (FFT) technique by using masking available in the Gatan DigitalMicrograph software package. Details of the microscope and the procedure applied in the study are described elsewhere [44].

For surface composition studies two X-ray photoelectron spectroscopy (XPS) apparatuses were used. The studies for fresh catalysts were performed using the multi-chamber ultra-high vacuum system (PREVAC) with a hemispherical Scienta R4000 electron analyzer. A Scienta SAX-100 X-ray source (Al Kα, 1486.6 eV, 0.8 eV band) equipped with the XM 650 X-Ray Monochromator (0.2 eV band) was used as complementary equipment. The pass energy of the analyzer was set to 200 eV for survey spectra (with a 500 meV step), and 50 eV for regions (high-resolution spectra): Co 2p, O 1s, Si 2p, Al 2p, and C 1s (with 50–100 meV step). The base pressure in the analysis chamber was $5 \cdot 10^{-9}$ mbar, and during the collection of spectra, it was not higher than $3 \cdot 10^{-8}$ mbar. To register XPS spectra for reduced catalysts, quasi *in situ* X-ray photoelectron spectroscopy studies were performed. The samples were placed in the load lock, degassed for 16 h, and transferred through the distribution chamber to the analysis chamber. After the first measurements (before reduction), the samples were transferred to the flow reactor chamber coupled to the ultra-high vacuum system. The samples were then reduced in the flow of a mixture consisting of H_2 (40 ml min^{-1}) and Ar (60 ml min^{-1}) for 60 min (p = 1 bar) at 500 °C. The temperature of the samples was measured with a thermocouple mounted inside the sample holder and controlled by a HEAT2-PS power supply. The samples were then cooled down, the gas mixture was pumped out, and, under vacuum conditions (without exposure to air), the whole holders were transferred to the analytical XPS chamber, where the next set of spectra was collected. The pass energy of the analyzer was set to 200 eV for survey spectra (with 750 meV step), and 50–100 meV for regions (high resolution spectra): O 1s, Co 2p, C 1s (before reduction). The state of the spent catalysts was evaluated *ex situ* using XPS analysis with a SESR4000 analyzer (Gammadata Scienta) in a vacuum chamber with a base pressure below $5 \bullet 10^{-9}$ mbar. Monochromatized Al-Kα source with 250 W at 1486.6 eV emission energy was used. The pass energy for selected narrow-range binding energy scans was 100 eV. The binding energy scales were corrected for the gold work function determined in the spectrometer, 4.65 eV. CasaXPSsoftware (v 2.3.23 PR1.0) was used for processing all XPS data [45]. The Co $2p_{3/2}$ XPS spectra before and after the *in situ* reduction were fitted with sets of curves characteristic for Co_3O_4 (before the reduction), and CoO and Co^0 (after the reduction). The line shapes and relative shifts of the peaks were taken from the reference [46].

Raman spectra of the spent catalysts were collected in the range of 1000–2000 cm^{-1} using Renishaw InVia spectrometer equipped with a 514 nm laser with a resolution of 1 cm^{-1}. For each spectrum, ten scans were accumulated.

The oxidation of the carbon deposit formed during the ESR process was studied by thermogravimetric analysis (TGA) using a TGA/DSC 1 Mettler Toledo apparatus. 10 mg of the spent catalyst powder was placed in an alumina crucible and weighted with a Mettler Toledo balance. The oxidation of the coke deposit was carried out in a temperature range of 30 to 800 °C at the heating rate of 10 °C min^{-1} under an air flow (80 ml·min^{-1}).

2.4. Catalytic tests

The performance of the reduced materials in the ESR process conditions (500 °C, molar ratio ethanol/H_2O of 1:12, WHSV = 52 h^{-1}) was analyzed by the application of a packed-bed quartz microreactor using catalyst testing equipment (PID Eng & Tech) and two gas chromatographs (Bruker 450-GC and Bruker 430-GC) according to the procedure described earlier [47]. To evaluate the catalytic activity, short-term (21 h) and long-term (>160 h) tests were performed.

The conversion of ethanol (X_{EtoH}) and the selectivity to carbon-containing products (X_{CP}) were determined from:

$$X_{EtOH} = \frac{C^{in}_{EtOH} - C^{out}_{EtOH}}{C^{in}_{EtOH}} \times 100\% \quad (1)$$

$$X_{CP} = \frac{n_i C^{out}_i}{\sum n_i C^{out}_i} \times 100\% \quad (2)$$

where: C^{in}_{EtoH} : - is the molar concentration of ethanol in the reaction mixture (mol%); C^{out}_{EtOH}- is the molar concentration of ethanol in the post-reaction mixture (mol%); C_i^{out} - is the molar concentration of the carbon-containing product in the post-reaction mixture (mol%); n – is the number of carbon atoms in a carbon-containing molecule of the reaction product.

The selectivity to hydrogen was calculated from:

$$H_2 selectivity = \frac{C^{out}_{H_2}}{C^{out}_{H_2} + 2 \times C^{out}_{CH_4} + 2 \times C^{out}_{C_2H_4} + 2 \times C^{out}_{CH_3CHO} + 3 \times C^{out}_{C_2H_6} + 4 \times C^{out}_{C_3H_8}} \times 100\% \quad (3)$$

where: C^{out} - is the molar concentration of the hydrogen-containing products in the post-reaction mixture (mol%). The carbon balance was within ±7% for all catalytic runs.

2.5. Operando UV–Vis and FT-IR studies of catalysts reduction, ESR process, and coke burning-off from used catalysts

The catalysts were formed in a self-supported pellet (20 mg) and placed in a spectroscopic cell. For UV–Vis studies, the Praying Mantis™ cell was used. For FT-IR studies the HT-IRS 01 cell was used (MeasLine, www.measline.com, Patent no. PL 232633). The gases to spectroscopic cells were introduced by 1/16" Teflon lines, kept at 110 °C. The activation of catalysts was performed under a flow of He (45 ml/min) with a heating rate of 30 °C/min from RT to 550 °C and the temperature was kept for 45 min. Then the catalyst was cooled down to 500 °C to perform the reduction under a flow of 10 %H_2/He (45 ml/min) for 120 min. Finally, the ESR reaction was performed at 500 °C for 2 h. The ethanol and water were introduced to a spectroscopic cell with a total flow of helium as carrier gas equal to 45 ml/min, and a molar ratio of ethanol/H_2O of 1:12. The ethanol and water containers were kept under constant and controlled temperature (23.4 °C). The activation, reduction, and reaction processes were followed with the use of either Shimadzu UV-2600 or Vertex 70 Bruker FT-IR spectrometers. Gas chromatography (Agilent Technologies 7890B) and mass spectrometry (MEASLINE RGA200) were used to assess the reaction products. After the catalytic reaction, the spectroscopic cell was cooled down to 250 °C. To assess the nature of the formed carbon deposit the 10 %O_2/He gas mixture was introduced (30 ml/min) and the temperature was gradually increased to 300, 350, 400, 450, 500, 550, 600, and 650 °C with a rate of 10 °C/min, at each step the temperature was stabilized for 15 min. The outlet gas composition was followed by mass spectrometry (m/z = 2 (hydrogen), 18 (water), 28 (carbon oxide, ethylene), 29 (acetaldehyde), 31 (ethanol), 44 (carbon dioxide), 16 (methane), 43 (acetic acid)). Total deposit removal was performed for 160 min.

3. Results and discussion

3.1. Catalysts performance for ethanol steam reforming: Effect of aluminium content, morphology of the support, and potassium presence

The studied samples Co|Z(32), Co|Z(750), and Co|Z(∞)-S varied in Al content corresponding to Si/Al = 32, 750, and ∞ (Al-free), respectively. On the other hand, the comparable content of the cobalt phase was achieved and was equal to 10.5 ± 1.5 wt% according to the XRF studies (Table S.1). The catalysts were studied for the ethanol steam reforming process in the conditions of 500 °C, ethanol/H_2O molar ratio of 1:12, and 21 h. The results concerning ethanol conversion and all product selectivity over time are presented in Fig. S1. As expected, the activity of the catalysts depends strongly on the Si/Al ratio of the zeolite support. For clarity, in Fig. 1 we present the conversion of ethanol and selectivity to the products most influenced, and at the same time, the

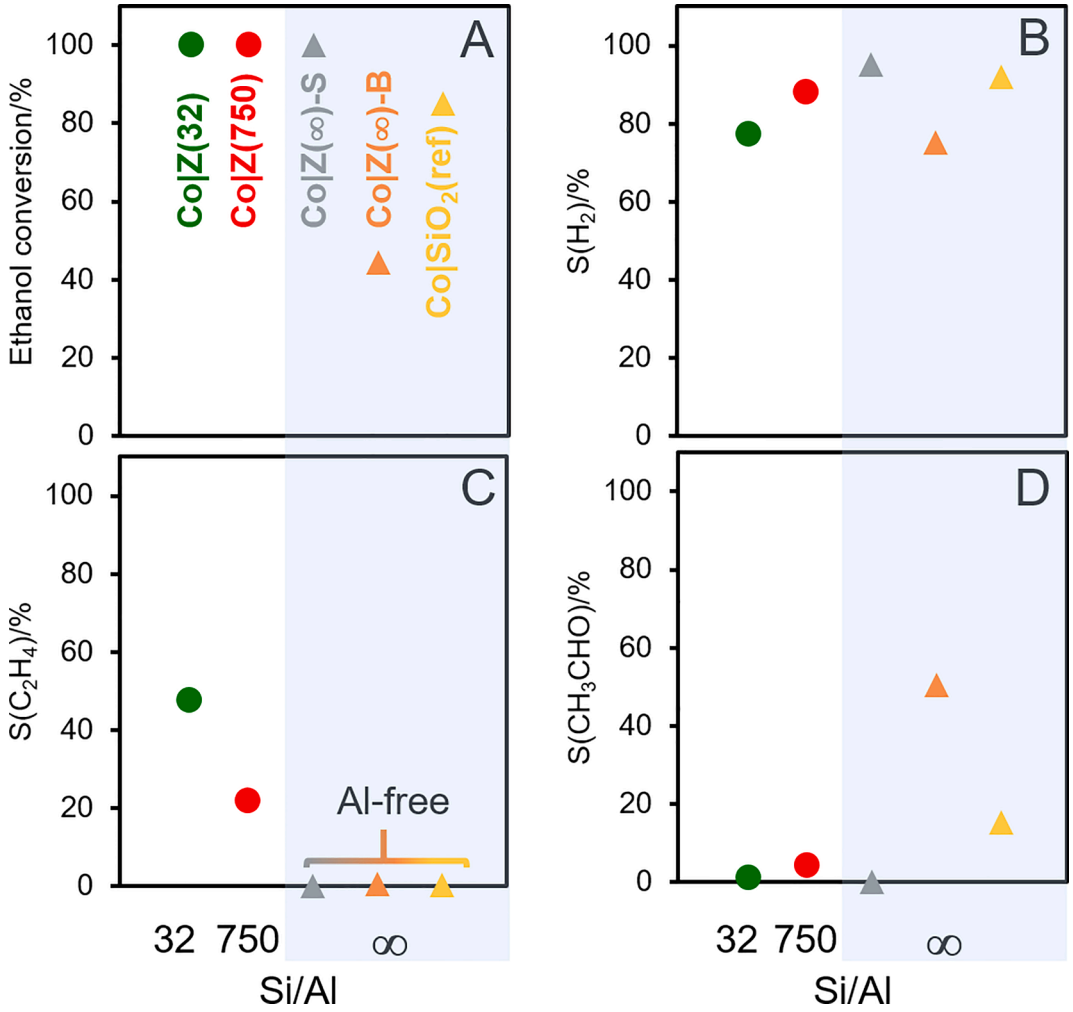

Fig. 1. The ethanol conversion (A) and selectivity to H_2 (B), C_2H_4 (C), and CH_3CHO (D) products in 21st hour of the ESR reaction at 500 °C for ethanol/H_2O molar ratio of 1:12 for the series of cobalt catalysts supported on ZSM-5 zeolite differing in Si/Al and crystal size. The Co|SiO_2(ref) serves as a reference system.

most important H_2, C_2H_4, and CH_3CHO in the 21st hour of the ESR process versus the Si/Al ratio. Firstly, we can see in Fig. 1A that under applied conditions the conversion of ethanol is equal to 100% for three catalysts, Co|Z(32), Co|Z(750), and nanometric Co|Z(∞)-S, independently from the Si/Al ratio (32 - ∞). At the same time, we observed significant differences in selectivity to H_2 and C_2H_4 for these samples. The selectivity to H_2 increases almost linearly with increasing of Si/Al from about 78% to 100% (Fig. 1B). In turn, selectivity to C_2H_4 decreases linearly from almost 50% for Co|Z(32) to about 20% for Co|Z(750), eventually disappearing completely for Al-free catalyst (Fig. 1C).

Bearing in mind the best catalytic behavior of Al-free material, Co|Z(∞)-S, we decided to evaluate the influence of the zeolite crystal morphology on the catalytic performance of the cobalt-containing catalyst. In general, the textural properties of all zeolite supports were preserved after impregnation with cobalt. The cobalt phase also did not plug the micropores of the zeolites, as confirmed by retained micropore volume for all the catalysts (Table S1).

The catalytic tests for the Co|Z(∞)-B catalyst, based on micrometric pure silica ZSM-5 zeolite, and for the Co|SiO_2(ref) catalyst, based on the reference micrometer-sized counterpart, were performed. The results for Co|Z(∞)-B and Co|SiO_2(ref) samples do not fit the trend previously observed for zeolites of varied Al content (Fig. 1). The conversion of ethanol for Co|Z(∞)-B reaches about 40% with the lowest selectivity to H_2 (below 80%) and the highest selectivity to undesired CH_3CHO (above 50%). Furthermore, the conversion of ethanol over the Co|SiO_2(ref) catalyst does not reach 100%, while CH_3CHO is produced with a selectivity of about 15%. The catalytic performance observed for these pure silica materials, Co|Z(∞)-B and Co|SiO_2(ref), diverges from that of nanometric Co|Z(∞)-S. Neither amorphous silica support nor crystalline pure silica micrometer-sized assure as high activity as the catalyst based on nanometric zeolitic support. The significant production of CH_3CHO over Co|Z(∞)-B and Co|SiO_2(ref) catalysts was previously assigned to a very weak interaction between the surface of the catalyst and acetaldehyde, resulting in the rapid release of undesired intermediates from the catalyst surface [47]. Thus, the effect of morphology becomes obvious when the performance of the nanometric (260 nm) Co|Z(∞)-S and micrometer-sized (50–90 μm) Co|Z(∞)-B catalysts are compared. Indeed, the dispersion of the cobalt phase is significantly better over the Z|(∞)-S zeolite support (Fig. S2) which is provided by its superior nanometric morphology. Thus, both the Al content and morphology of the zeolite support must be adjusted to develop an efficient catalyst for the ESR process.

The positive effect of alkali on the ESR process has been widely reported for many oxide-based catalysts. Therefore, we hypothesized a synergic effect of the potassium doping and the limited presence of aluminium atoms (Brønsted and Lewis acid sites) in the commercially available Z(750). To analyze the role of the potassium promoter we compared the catalytic activity in the ESR process of the Co|Z(750) catalyst and its potassium-containing counterparts (Fig. S3). The latter were prepared via two different routes resulting in the location of K^+ cations either in extra-framework positions in Co|Z(750)-IE or potassium oxo-species dispersed on the external surface of Co|Z(750)-IWI. The results are consistent with our previous results [10] reporting the drawback of the addition of alkali on the ethanol conversion in ESR. Namely, the total ethanol conversion of the Co|Z(750) catalyst decreased to c.a. 90 %, and 10 %, for Co|Z(750)-IE and Co|Z(750)-IWI, respectively. However, at the same time, the selectivity to undesired C_2H_4 dropped down from 22 to 15% for Co|Z(750)-IE while not occurring for Co|Z(750)-IWI (Fig. S3). The elimination of the dehydration path of the ESR process can be significantly limited or eliminated by potassium addition [10]. Although the ESR results of the potassium modification with the ion-exchange approach are promising, still the Co|Z(750)-IE sample cannot compete with the Al-free Co|Z(∞)-S sample without potassium, pointing to the importance of both the absence of Al-atoms and nanometric character of zeolitic support.

The stability test (the 160 h ESR reaction) was next carried out for the most promising pure silica zeolites Co|Z(750) and Co|Z(∞)-S and non-zeolitic Co|SiO_2(ref) catalyst as the reference system. The full experimental data for long-term stability tests are presented in Fig. S4, while the comparison of the ethanol conversion and selectivity to products at 160 h of the tests are presented in Fig. 2. The results excluded the Co|SiO_2(ref) as being able to compete with Co|Z(750) and Co|Z(∞)-S owing to a progressive decrease in ethanol conversion.

In contrast to amorphous support, Co|Z(750) and Co|Z(∞)-S catalysts exhibited excellent ESR long-term performance. The Co|Z(750) catalyst preserved 100% conversion, and almost 95% selectivity to H_2 during the whole 160 h of the catalytic test. The selectivity to C_2H_4 at a 20% level can be considered its disadvantage since ethylene is the primary coke precursor. Still, the results are outstanding compared to the current state of the art [32,36]. From the several dozen catalysts compared in [32,36] only a few cobalt catalysts based on CeO_2 support exhibited ethanol conversion equal to 100% and selectivity to hydrogen $>$ 90% at 500 °C. It has to be underlined, that most studies concern short-time activity tests, which do not show the stability of the system. Whereas, stability in the ESR process is a crucial point considering the carbon deposit formation leading to catalyst deactivation in time. In turn, no C_2H_4 was produced over the Co|Z(∞)-S catalyst. Nonetheless, a slight decrease in the ethanol conversion appears after 80 h on stream, leading to a value of about 90%.

The strong impact of the number of Al atoms and zeolite morphology on the performance of the Co-containing zeolite-supported ESR catalysts was then thoroughly evaluated in terms of their acidity (FT-IR sorption studies), reducibility (H_2-TPR), phase composition (XRD), morphology (SEM, HR-TEM/EDX), and surface redox properties (*in situ* XPS, phase separation with FFT). Detailed information on the ESR reaction mechanism was acquired in unique *operando* UV–Vis and FT-IR spectroscopy studies. Furthermore, the comprehensive characterization of spent catalysts was carried out to examine the deactivation process.

3.2. The interplay between the nature and dispersion of the cobalt species and catalyst performance

The Co|ZSM-5 catalysts varied in Al atoms number and their Co-free counterparts were examined in quantitative pyridine (Fig. 3A and Fig. S5) and CO (Fig. 3B) sorption FT-IR studies to provide complete insight into the nature of surface sites involved in the interaction with ethanol during the ESR process. The presence of both Brønsted and Lewis acidic sites in the zeolite Z(32) is documented by the bands of pyridinium ions, PyH^+ (1545 cm^{-1}), and pyridine bonded coordinatively to the Lewis site, PyL (1445 cm^{-1}). Quantitatively, the acid sites density decreased significantly in Z(750) and the purely siliceous material Z(∞)-S. Both materials exhibit a marginal number of Brønsted and Lewis acid sites (Table 1). The deposition of the cobalt phase on the zeolitic supports resulted in the notable reduction of Brønsted property, while new electron acceptor cobalt-derived species appeared, i.e. Co^{2+} cations and/or CoO_x^{y+} oxo-species, replacing protons from Si(O^-)Al units. Such a decline in the number of Brønsted acid sites is responsible for hampering the ethanol dehydration path leading to undesired ethylene. The dispersion of cobalt species was tentatively assessed from Py sorption studies. By assuming that the deposition of the cobalt phase implies the appearance of an additional number of Lewis centers without affecting the native Lewis sites, the concentration of cobalt sites was calculated as the difference between the number of Lewis centers in the Co- and H-zeolites (Table 1). The highest concentration of Lewis sites was found for Co|Z(32) and Co|Z(∞)-S. The highest ion-exchange capacity of Co|Z(32) allows us to anticipate the positively charged cationic cobalt species neutralizing the charge of the zeolite framework as the major ones.

In contrast, in Co|Z(∞)-S, the presence of Lewis acidic sites is expected to be related to the metallic cobalt phase. Indeed, the highest population of cobalt-derived Lewis sites in the Co|Z(∞)-S catalyst implies their highest dispersion and corresponds well to the catalyst's best

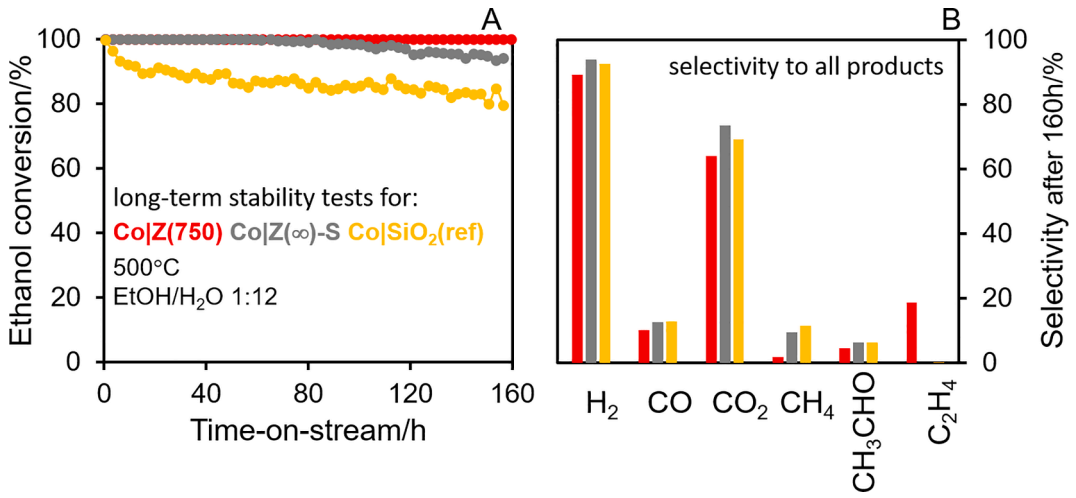

Fig. 2. A) Stability of the ethanol conversion for the Co|Z(750) (red column), Co|Z(∞)-S (gray column), and Co|SiO_2(ref) (yellow column) catalysts in the ESR reaction at 500 °C for ethanol/H_2O molar ratio of 1:12. (B) Selectivity to products after 160 h of the process. (For interpretation of the references to colour in this figure legend, the reader is referred to the web version of this article.)

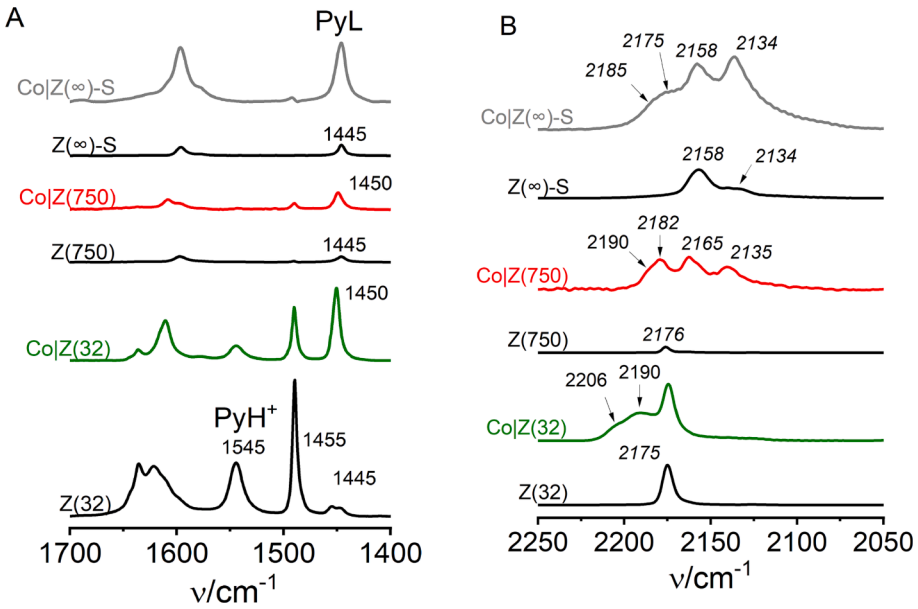

Fig. 3. The FT-IR spectra of pyridine (A) and CO (B) adsorbed on Co|Z(32), Co|Z(750), and Co|Z(∞)-S catalysts and corresponding zeolite supports.

ESR performance.

The carbon monoxide molecule is the first-choice probe molecule used as the descriptor of the properties of surface redox sites and their dispersion, also in a quantitative manner. Ligation of CO to redox sites results in the appearance of carbonyl bands, whose positions are indicators of the electron acceptor properties of the redox sites. The lower the frequency of the monocarbonyl band, the lower the electron acceptor properties of the cobalt species [10]. The spectra of CO interacting with Co|Z(32), Co|Z(750), Co|Z(∞)-S, and their H-counterparts are presented in Fig. 3B.

According to literature reports, the band at 2206 cm^{-1} observed solely in Co|Z(32) was ascribed to the CO molecule ligated to the isolated exchangeable cobalt(II) cations in the zeolite micropores. The interaction of CO molecules with cobalt oxo-sites is documented by the appearance of bands in the frequency range of 2190–2175 cm^{-1}. The increased amount of cobalt oxo-species and the notable shift of the respective bands to the lower frequency is related to oxolation processes facilitated by marginal or absent Al atoms in zeolites. Quantitative FT-IR studies of CO sorption confirmed also the weakening of the electron acceptor properties of cobalt centers with the increase of the Si/Al value, which was further manifested as the decline in the number of centers capable of binding the CO molecule (Table 1). The additional maxima in the frequency range of 2165–2135 cm^{-1} can be assigned to Co^{+}(CO) species [48]. Some authors, however, assigned these bands to CO hydrogen-bonded to silanol groups terminating the zeolite crystals (2165 and 2158 cm^{-1}) and to physisorbed CO (2134 cm^{-1}) [49]. The absence of carbonyls typical of metallic cobalt (at 2085–2000 cm^{-1} - linear carbonyls of metallic cobalt, and at 1880 cm^{-1} - bridging carbonyls of Co^0) could be indicative of very low heat of adsorption of CO on cobalt sites dispersed on zeolitic supports.

Inspection of the data derived from quantitative FT-IR studies of CO and Py sorption reveals some divergence among the number of Lewis sites detected with CO and Py which is assigned to an extensive difference in the basicity of the probe molecules (gas basicity of 898.1 for Py vs. 402.2 kJ/mol for CO). Py as a stronger base can probe sites with significantly lower acidic properties compared to those of a less basic CO

Table 1
The concentration of Brønsted (B), and Lewis (L) acid sites, the concentration of Co species (Co^{2+} ions and oxide-like cobalt forms – OLC) for Co|Z(32), Co|Z(750), Co|Z(∞)-S and Co|SiO_2(ref) catalysts and corresponding supports.

Sample	Al[a]	B[b]	L[b]	B + L[b]	Co-originated Lewis acid sites			
					$Co_{(Py)}$[c]	$Co^{2+}_{(CO)}$[d]	$OLC_{(CO)}$[d]	$(Co^{2+} + OLC)_{(CO)}$[d]
	μmol·g^{-1}				μmol·g^{-1}			
Z(32)	472	*445*	*70*	*475*	–	–	–	–
Co|Z(32)		**247**	**328**	**575**	**258**	**62**	**77**	**139**
Z(750)	15	5	5	10	–	–	–	–
Co|Z(750)		**0**	**68**	**68**	**63**	**0**	**57**	**57**
Z(∞)-S	*0*	*0*	*5*	*5*	–	–	–	–
Co|Z(∞)-S		**0**	**315**	**315**	**310**	**0**	**65**	**65**
SiO_2(ref)	*0*	**0**	**0**	**0**	**–**	**–**	**–**	**–**
Co|SiO_2(ref)		**0**	**3**	**3**	**3**	**0**	**3**	**3**
Z(∞)-B	**0**	The size of the grains makes it impossible to register the spectrum in the transmission mode, i.e. in the mode that allows for quantitative interpretation of the spectrum						
Co|Z(∞)-B	**0**							

[a] The concentration of Al from ICP analysis.
[b] The concentration of Brønsted (B) and Lewis (L) acid sites determined by FT-IR studies of pyridine adsorption.
[c] The concentration of cobalt sites able to interact with Py calculated as the difference between the number of Lewis acid sites in Co|Z and HZ.
[d] The concentration of Co^{2+} ions (2206 cm^{-1}) and oxide-like cobalt forms (OLC) determined by CO adsorption FT-IR studies (the 2190–2178 cm^{-1} band).

molecule. Furthermore, the high concentration of the cobalt acid sites interacting with Py in Co|Z(∞)-S suggests high dispersion of the cobalt active phase since electron-deficient metal moieties can also serve as the sites for Py adsorption [50]. FT-IR spectroscopy evidenced that the number of nitrogen-coordinated pyridine chemisorbed perpendicularly to the surface of the metal nanoparticles [51] gives rise to 1460–1445 cm^{-1} IR bands, especially when the surface electron density of the metallic phase decreases when dispersed on acidic supports such as zeolites. Thus, fine-tuning the acidic properties of the ZSM-5 support by the decrease of Al content can significantly reduce or even completely rule out the production of undesired C_2H_4 with accompanying improvement of the H_2 efficiency.

The XPS analysis of the samples before and after *in situ* reduction reveals extensive changes in the cobalt phase located on the external surface and subsurface of the catalysts grains (Fig. 4). For all materials the initial spectra present the features characteristic of the Co_3O_4 phase (curves denoted a, pink shading). *In situ* reduction transforms a major part of cobalt into a metallic phase, however, some CoO is still present (curves b, blue and yellow shading respectively). The extent of reduction is the highest for the Co|Z(∞)-S sample whereas the supports containing Al atoms kept a similar share of the CoO phase. The presented results indicate that the cobalt oxidation state can be tuned by the acidic property of the zeolite support.

Surface, subsurface, and bulk are usually considered separate entities due to the difference in the interaction of the active phase with the zeolite environment. The XPS measurements provide information about the nature of the cobalt phase located on the outer and subsurface surfaces, thus the picture of the catalysts' reducibility was complemented in H_2-TPR investigations (Fig. 5).

According to the literature, the maxima at lower temperatures are assigned to the reduction of Co^{3+} to Co^{2+} while the reduction of Co^{2+} to Co^0 requires higher temperatures [52]. The Co|Z(∞)-S catalyst presents the reduction peaks located in the lowest temperature range of about 200 to 350 °C with an important share of maximum at 275 °C. Based on XPS data, in Co|Z(∞)-S the reduction process is effective thus the cobalt metallic species are dispersed on the outer surface of the nanometric support in the majority [10]. With increasing Al concentration (Co|Z(750) and Co|Z(32)) the lower share of metallic phase, detected with

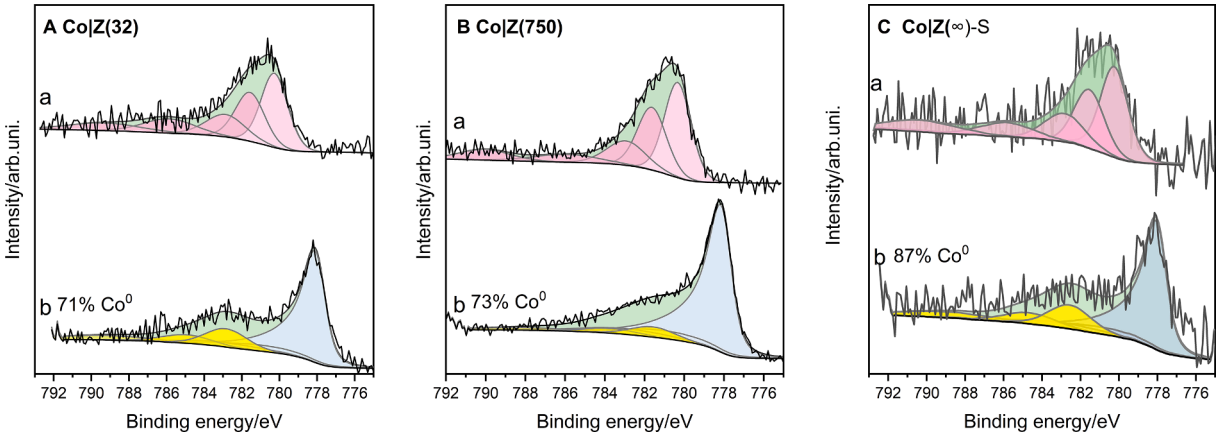

Fig. 4. XPS spectra of Co 2p core level collected for as received and after quasi *in situ* reduction of the Co|Z(32) (A), Co|Z(750) (B), Co|Z(∞)-S (C) catalysts (H_2 (40 ml min^{-1}) and Ar (60 ml min^{-1}) over 60 min (p = 1 bar) at 500 °C). Color shading designates components of Co 2p spectra due to different oxidation states of cobalt: pink – Co_3O_4; yellow – CoO; blue Co^0. (For interpretation of the references to color in this figure legend, the reader is referred to the web version of this article.)

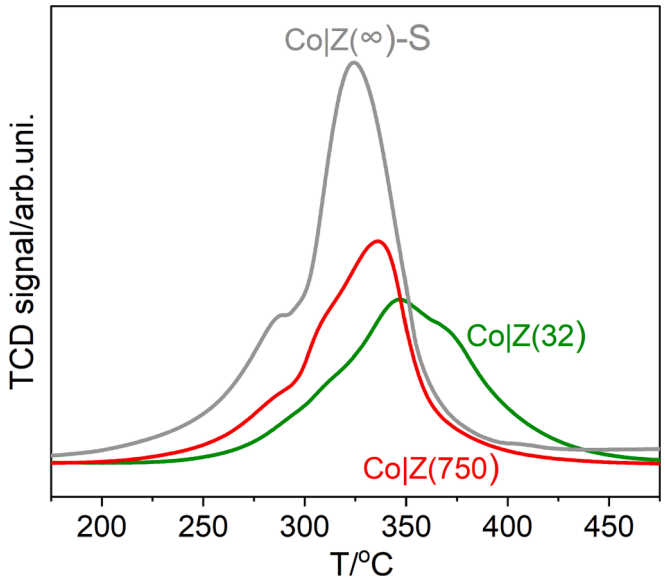

Fig. 5. H_2-TPR profiles of the Co|Z(32), Co|Z(750), and Co|Z(∞)-S catalysts.

XPS data, is associated with the increase in the temperature of the reduction process, as documented in the TPR profiles. These findings indicate that acidic functions of the zeolitic supports have a negative impact on the dispersion of the cobalt phase. Further, the highest overall hydrogen consumption for Co|Z(∞)-S equal to 2.913 mmol·g^{-1}, is significantly higher compared with 1.808 and 1.568 mmol·g^{-1} for Co|Z (32) and Co|Z(750) catalysts, respectively. As a result, the XPS and TPR data suggest that in Al-containing supports the oxo-species are still present and the the cobalt phase is not completely reduced. The non-reduced cobalt oxo-species are anticipated to be located inside bigger cobalt grains as the micropore volume values are not affected by cobalt phase deposition (Table S1).

The lack or the minor share of the cobalt phase lines in the diffractograms (Fig. S6) indicate its high dispersion either amorphous nature in the as-prepared catalysts [8]. Additional microscopic characteristics were therefore conducted to reveal the nature and location of the cobalt species in reduced catalysts. Representative HR-TEM images of the reduced Co|Z(32), Co|Z(750), and Co|Z(∞)-S catalysts with the corresponding FFT and phase identification are presented in Fig. 6 (additional microscopic characteristics in Fig. S7). In general, the cobalt phase nanograins are well dispersed on the surface of all zeolite supports (see Fig. S7). For the Co|Z(32) and Co|Z(∞)-S catalysts the size distribution of the cobalt nanograins in the range of 10–50 nm is observed. The absence of Al-atoms in the Z(∞)-S zeolite framework together with its nanometric characteristic results in the share of metallic cobalt of the grain size below 5 nm (Fig. 6C and Fig. S7C_3). In turn, for the Co|Z(750) sample small 10–50 nm nanograins coexist with a small amount of much bigger ones, even with a size of about 200 nm. As shown in XPS and TPR studies the highest catalytic activity can be ascribed to the material offering the cobalt phase of the highest dispersion and reducibility. Therefore the species below 5 nm are identified as the most active in the ESR process. Furthermore, FFT analysis indicates a significant difference in the oxidation state of cobalt.

In the case of Co|Z(32) cobalt was present mainly in the form of CoO (Fig. 6A1-A3) identified based on the distances of 2.12 and 2.46 A, corresponding to the (200) and (111) facets, respectively. For Co|Z (750), both CoO and metallic Co were identified based on the distances of 2.12, 2.46 A, and 1.77 A corresponding to the (200) and (111) facets of CoO and the (200) facet of Co, respectively (Fig. 6B1-B3). In turn, only the metallic phase of cobalt was identified for the Co|Z(∞)-S catalyst based on interplanar distances of 1.91, 1.80 A, and 2.05 A corresponding to the (011), (002), and (111) facets of Co metal, respectively (Fig. 6C1-C3). The lack of Al-framework atoms makes the cobalt oxo-forms prone to reduction to metallic species because the cobalt cations are not stabilized by the negative charge of the zeolite framework. The microscopic observations are in line with the H_2-TPR and FT-IR findings about the superior cobalt phase dispersion for Co|Z (∞)-S catalyst.

3.3. Operando UV–Vis and FT-IR spectroscopy investigation of the catalysts reduction and the ESR reaction.

The *operando* UV–Vis studies under reducing conditions (Fig. 7A) and under the ESR reaction conditions were carried out for Co|SiO_2(ref), Co|Z(∞)-S, and Co|Z(750) samples. The band assignment was based on the literature survey described in detail in ESI. The spectra in Fig. 7A show changes in the speciation of cobalt forms upon the reduction of the catalysts at 500 °C. For Co|SiO_2(ref) the flow of hydrogen causes a decrease in the intensity of the bands located at 680 nm (reduction of Co^{3+}) and 450 nm (reduction of Co^{2+}) documenting the reduction of the Co_3O_4 phase [53]. The reduction of Co^{3+} cations precedes the reduction of Co^{2+}, manifested by the disappearance of the 460 nm band before the band at 680 nm. The noticeably smaller abundance of Co^{3+} sites in Co|Z (∞)-S than in Co|SiO_2(ref) may be explained by a more efficient initial reduction of spinel in the nitrogen atmosphere. The $O^{2-}(2p) \rightarrow Co^{2+}$ band at 300–450 nm disappears upon prolonged contact with hydrogen indicating efficient oxo-phase reduction. Also, the process of Co|Z(750) reduction involves the disappearance of a band triplet in the visible region between 400 and 750 nm. The presence of framework aluminium species, even to a marginal extent, facilitates the preservation of α-Co$(OH)_2$ and β-Co$(OH)_2$ species identified by the absorption band at 780–800 nm.

An inspection of the UV–Vis spectra indicates that almost complete reduction of the oxide phases occurred for the catalysts Co|Z(∞)-S and Co|Z(750) only while for Co|SiO_2(ref) some oxo-forms are resistant to H_2 treatment. These findings confirm that the nature of oxo-species strongly depends on the support that is further reflected in differentiated reducibility of the cobalt phase, as confirmed previously in H_2-TPR, HR-TEM, and FT-IR sorption studies.

The speciation of cobalt was monitored with UV–Vis also under *operando* ESR conditions (Fig. 7B). In Co|SiO_2(ref) the phenomenon of accumulation of polyaromatics as the precursor of carbon deposit is confirmed by $\pi \rightarrow \pi^*$ transitions at 650 nm band [54,55]. The band at 450 nm can arise from the accumulation of acetaldehyde species and the products of aldol transformations. On the Co|Z(∞)-S surface the ethanol dehydration route to ethylene, being a coke precursor, is inhibited by a lack of strong protonic sites. Therefore, the band at 220 nm appearing in the latter reaction course was attributed to the C=O units in acetaldehyde bonded to metallic Co species. For Co|Z(750) catalyst, its protonic acidity facilitates the formation of carbon deposit precursors, which in contrast to both former catalysts, originates from the ethylene oligomerization process, documented by the evolution of the bands of the C=C species at 230 nm. Indeed, similar bands have been reported during hydrocarbon oligomerization at elevated reaction temperatures on acidic zeolites [56,57]. In the later reaction period, the hydrogen-deficient highly-condensed aromatic structures are formed as documented by the evolution of 780 nm in the late reaction course.

The nature of the species adsorbed on the surface of the catalysts was monitored in *operando* ESR conditions by employing FT-IR spectroscopy (Fig. 8). The reaction products were determined using gas chromatography and mass spectrometry (Fig. S8). The oscillation rotation spectrum centered at the 3018 cm^{-1} band, clearly visible for Co|Z(750), validates the dehydration on Brønsted acid sites for this catalyst. The dehydrogenation route leading to acetaldehyde is confirmed by the band of C-H stretching in aldehyde group C(H)=O at 2750 cm^{-1}, with the greatest intensity for Co|SiO_2(ref). In the case of Co|Z(750), both routes occur, however, the first of the paths disappears over time in favor of the second. The initial dominant share of ethylene becomes lower with time,

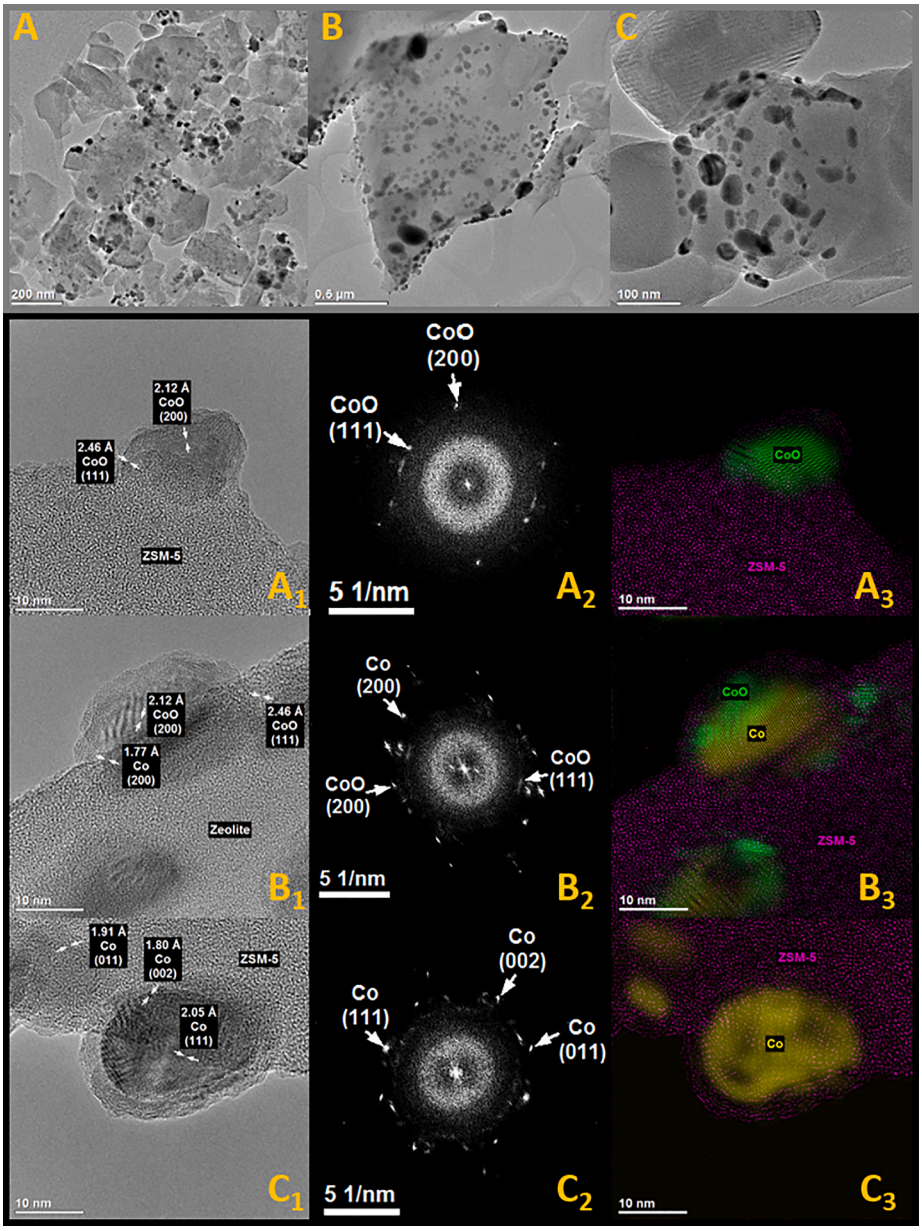

Fig. 6. TEM pictures of the Co|Z(32) (A), Co|Z(750) (B), Co|Z(∞)-S (C) catalysts after reduction with the phase identification for Co|Z(32) ($A_{2\text{-}3}$), Co|Z(750) ($B_{2\text{-}3}$), and Co|Z(∞)-S ($C_{2\text{-}3}$).

probably due to ethylene oligomerization and poisoning of the protonic sites by carbon deposit precursors, as documented in UV–Vis spectra.

The dehydrogenation path seems to be activated a bit later which is documented by increased intensities of the C(H)=O band in time for Co|Z(750). The advanced formation of acetaldehyde species in Co|Z(750), i.e. their rapid releasing from the catalyst surface is also proved by the lowest amount of CO_2 and CO confirmed by bands at 2350 cm^{-1} and in the region 2200–2000 cm^{-1}, respectively (see spectra in Fig. 8C2). The formation of carbon di- and monoxide can be referred to the decomposition of dominant species with signals at 1743, 1550, and 1440 cm^{-1} corresponding to the modes of acetic acid, acetates, and carbonates [58]. The latter peaks are accompanied by the C(H)=O band at 2735 cm^{-1}, which proves the origin of these compounds from the dehydrogenation path. Still, the highest intensity of acetate/carbonates species observed for Co|Z(750) allows for concluding their very high stability. Inhibition of the ethanol dehydration route is well observed for Co|Z(∞)-S and Co|SiO_2(ref) catalysts. While the acidity of silanols in Co|Z(∞)-S results in the formation of a marginal amount of ethylene, for the amorphous matrix only a dehydrogenation path is available. The production of actealdehyde, confirmed further by the very intense C=O bands (1770–1720 cm^{-1} band) is the most representative of Co|SiO_2(ref). More detailed inspection in the C=O frequency region allows also to conclude that in the first reaction period, acetaldehyde is very transformed into acetates which subsequently are decomposed to CO_2 and CO. Carbon dioxide can be stored on the surface as carbonate species. The conversion of acetaldehyde to carbonates is therefore determinant for the selectivity of the ESR process over Co|SiO_2(ref). It is in line with catalytic data when higher production of CO and CO_2 was detected for Co|SiO_2. As aforementioned, Z(∞)-S support provides some number of silanols of acidity high enough to launch the dehydration route in the initial period of the ESR process. Notably, both the FT-IR characteristics of ethylene (oscillation-rotation spectrum in 3200 – 2900 cm^{-1}) and aldehyde (2750 cm^{-1}) for Co|Z(∞)-S are of very weak intensity documenting their very low abundance. The spectrum of Co|Z(∞)-S is dominated by CO_2. The intermediate products (i.e. acetaldehyde, acetetes, carbonates) are poorly populated in the catalyst, as confirmed by

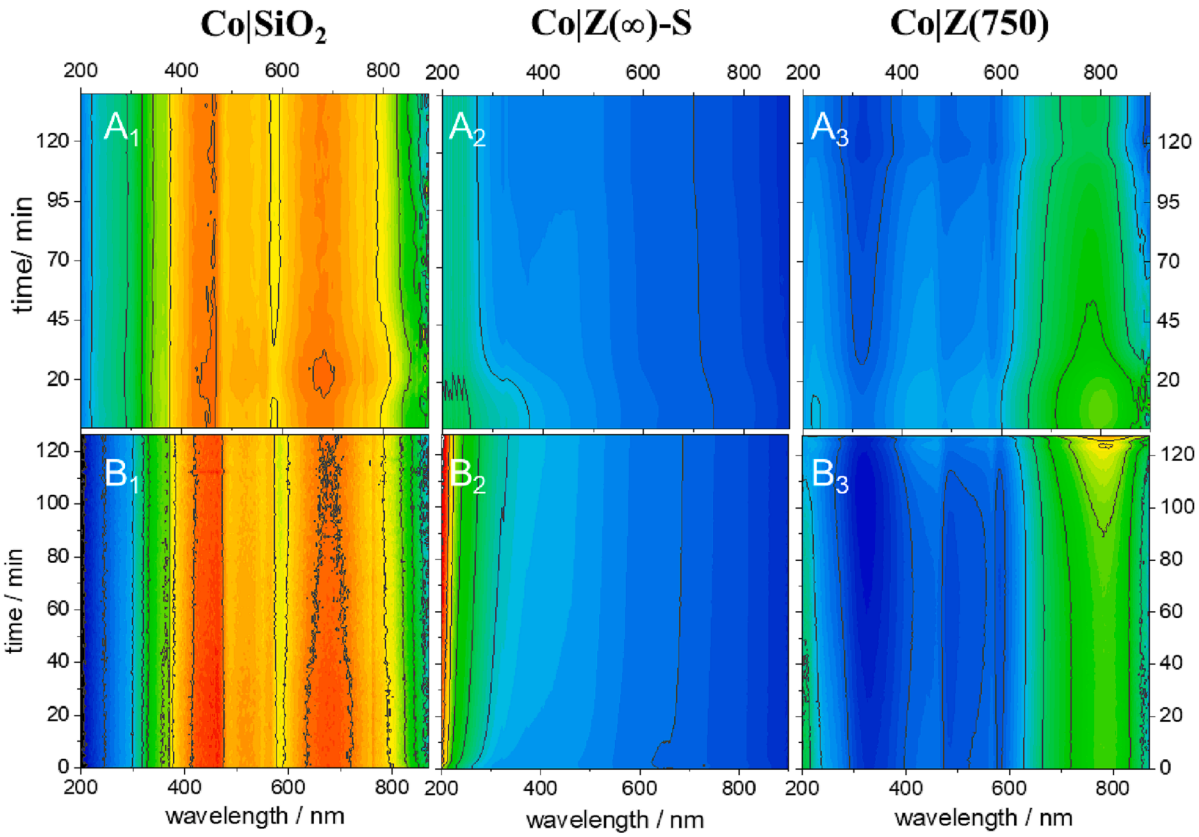

Fig. 7. UV–Vis spectra collected during (A) the reduction of the catalyst in H_2/He atmosphere at 550 °C for 2 h and (B) the ESR reaction monitored under *operando* conditions (C_2H_5OH: H_2O = 1:12, He flow, 500 °C).

their diagnostic bands of the lowest intensities among all the catalysts. Such behavior points to very efficient dehydrogenation of ethanol to acetaldehyde and a rapid very simultaneous oxidation of carbonates which are also effectively decomposed to produce the final reaction product. The findings from FT-IR spectra are corroborated by the profiles of the reaction products determined by gas chromatography and mass spectrometry (Fig. S8), which also match very well with the catalytic test results (see Section 3.1). For, Co|$SiO_{2(ref)}$ the selectivity to CH_3CHO (m/z = 29) and CO_2 (m/z = 44) increases while the selectivity to CO (m/z = 28) and H_2 (m/z = 2) decreases. For Co|Z(750) and Co|Z(∞)-S, the production of CH_3CHO stays constant, while the selectivity to CO and CO_2 decreases. This parallel decline in CO and CO_2 production may be associated with the ongoing formation of coke precursors in the dehydration pathway triggered by the presence of acid centers (Si(OH)Al or silanol groups). The influence of ethylene giving the impact to m/z = 28 mass signal on the trends observed is marginal. Gas chromatography analysis of reaction products (Fig. S8) confirms that Co|SiO_2(ref) has the highest yield to CH_3CHO and the lowest CO_2/CO ratio. The conclusions from *operando* spectroscopic studies confirm the interpretation of the ESR performance and physicochemical characterization results described above.

In Fig. 9 we presented the MS profiles of the products of the combustion of carbon deposit formed during *operando* FT-IR studies over highly active Co|Z(750) and Co|Z(∞)-S. From the course of the CO_2 evolution, we can anticipate the nature of coke precursors formed in the initial stage of the ESR reaction. The ethylene oligomers in Co|Z(750), which are burning off at lower temperatures, are dominant coke precursors. In Co|Z(∞)-S the coke precursors are formed to a lesser extent.

3.4. Carbon deposit characterization

The spent Co|Z(750) and Co|Z(∞)-S catalysts, maintaining the highest stability for 160 h under the ESR process conditions, were characterized in a microscopic and spectroscopic manner. A relatively small amount of loosely bonded carbon deposit in both catalysts is observed, however, with a visible lower quantity for Co|Z(∞)-S (Fig. 10A, B, more detailed TEM characteristic in Figs. S9 and S10) confirming that the coke deposit is primarily formed by ethylene secondary transformations. Also, the XPS analysis confirms the presence of carbon deposit on the surface of spent Co|Z(750) and Co|Z(∞)-S catalysts. For the Co|Z(∞)-S catalyst distinct signals of all Si, O, and C are observed (C 1s: 65%, O 1s: 23%, Si 2p: 12%), while only C 1s signal is observed for the Co|Z(750) catalyst, indicating significantly higher surface covering with carbon for the later (Fig. 11). The carbon units are located outside the zeolite crystals and do not block the cobalt active sites (see Figs. S9, S10). Thus, neither extensive covering with a carbon deposit of the whole Co|Z catalysts grains nor significant removal of the cobalt phase nanograins (observed in our previous work [47]) is an issue for the developed ESR catalysts. Nevertheless, there are some nanograins of cobalt active phase detached from zeolite support and enclosed inside the carbon deposit, e.g., at the tip of the carbon deposit filaments, being totally or partially enveloped (Fig. 10A3, A4, B3, B4).

The differences in the nature of the carbonaceous deposit formed on the Co|Z(750) and Co|Z(∞)-S catalysts noticeable in the microscopic images were further investigated by Raman spectroscopy and by thermogravimetry. The representative spectra are presented in Fig. 12A. Two intense Raman bands at 1600 and 1350 cm^{-1} are associated with the vibrational modes of graphitic carbon (G-band) and disordered/amorphous carbon (D-band), respectively [59]. The ratios of peak intensities I_D/I_G, serving as an indicator of the degree of graphitization of coke, are equal to 0.87 and 0.99 for Co|Z(750) and Co|Z(∞)-S, respectively. In addition, the sets of Raman spectra collected at various places of the samples are presented in Fig. S11. They show difference in homogeneity of the coke deposit formed over the Co|Z(750) and Co|Z(∞)-S

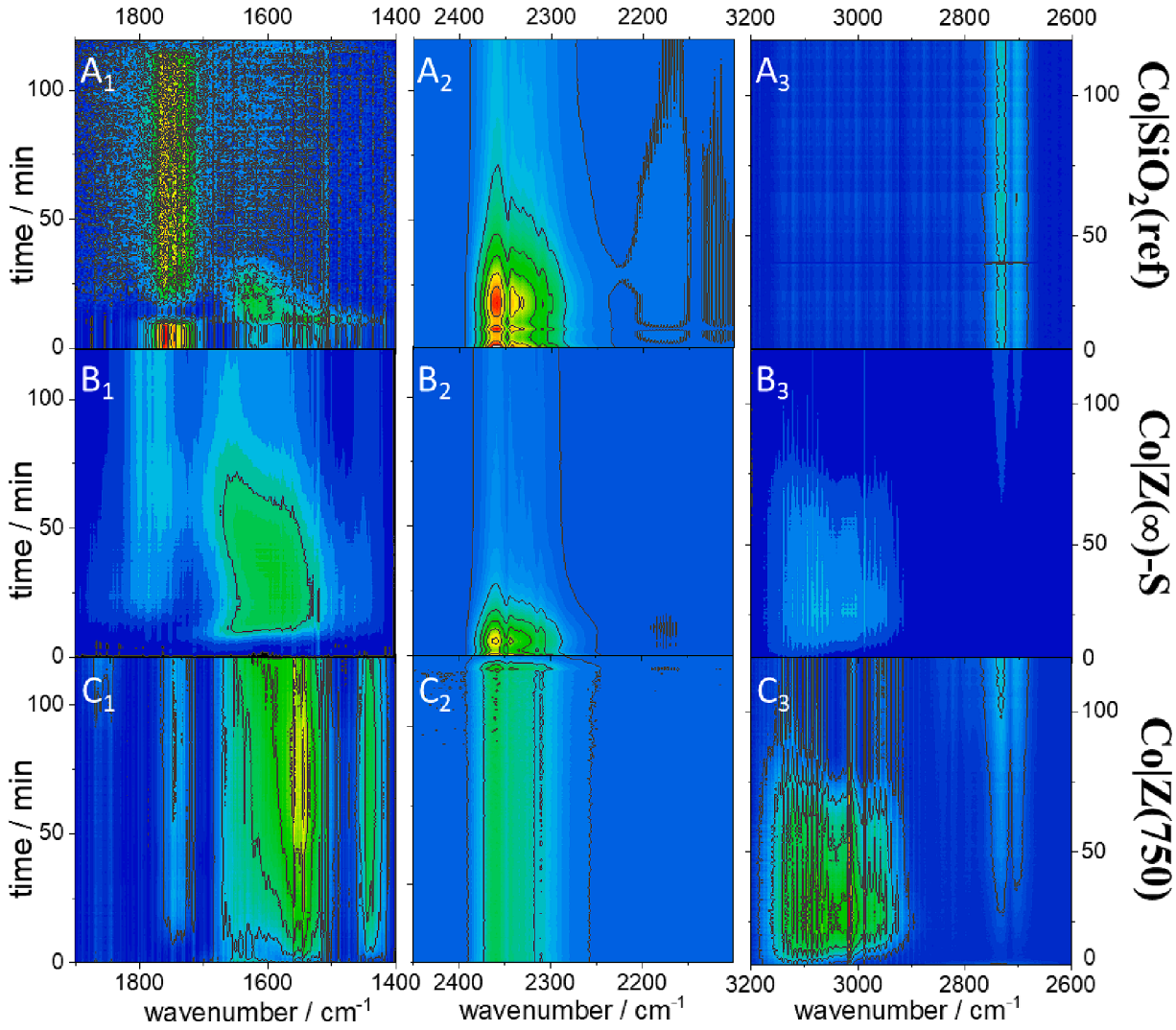

Fig. 8. FT-IR spectra collected during the ESR process (C_2H_5OH: H_2O = 1:12, N_2 flow, 500 °C) presented in C = O (A_1, B_1, C_1), CO_2 and CO (A_2, B_2, C_2), and C-H (A_3, B_3, C_3) stretching frequency regions for Co|SiO_2(ref), Co|Z(∞)-S, and Co|Z(750).

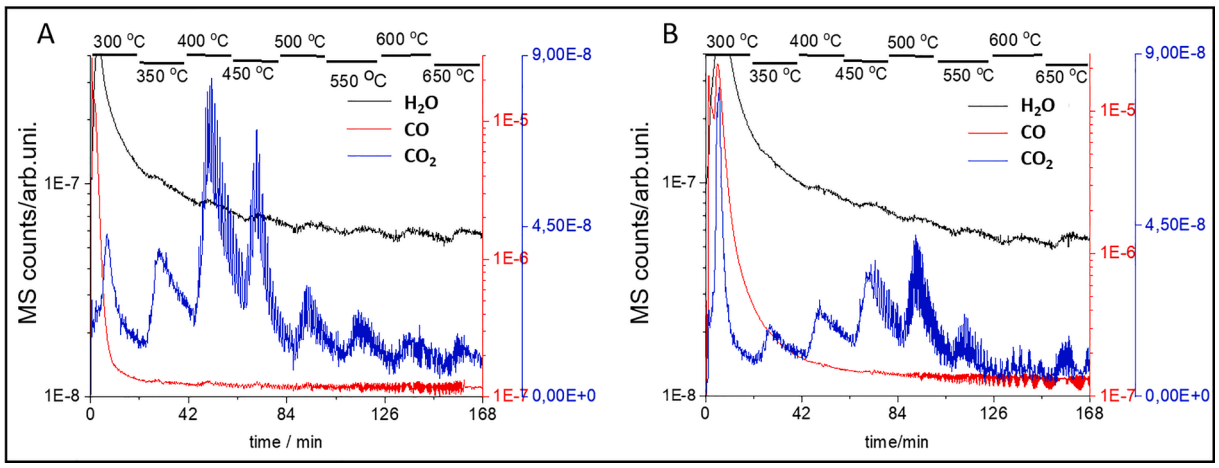

Fig. 9. MS profiles of the products (H_2O (dark line), CO (red line), and CO_2 (blue line)) gathered during the carbon deposit burning-off process after *operando* FT-IR studies of the ESR process over Co|Z(750) (A) and Co|Z(∞)-S (B) catalysts. (For interpretation of the references to colour in this figure legend, the reader is referred to the web version of this article.)

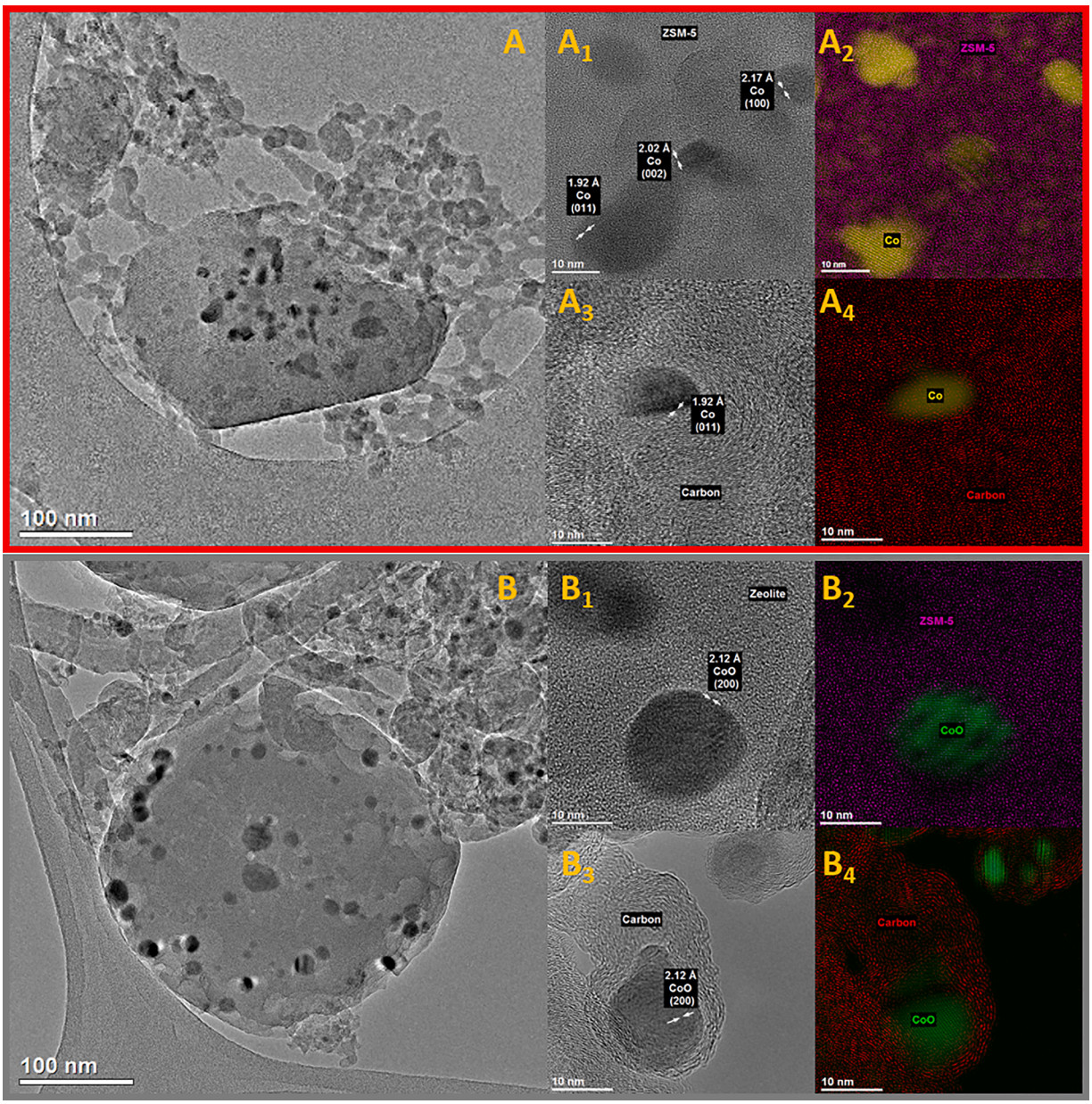

Fig. 10. Microscopic analysis of the Co|Z(750) (A) and Co|Z(∞)-S (B) catalysts after 160 h in the ESR process conditions (500 °C, EtOH:H_2O = 1:12). HR-TEM images (A_1, A_3, B_1, B_3), and phase identification (A_2, A_4, B_2, B_4).

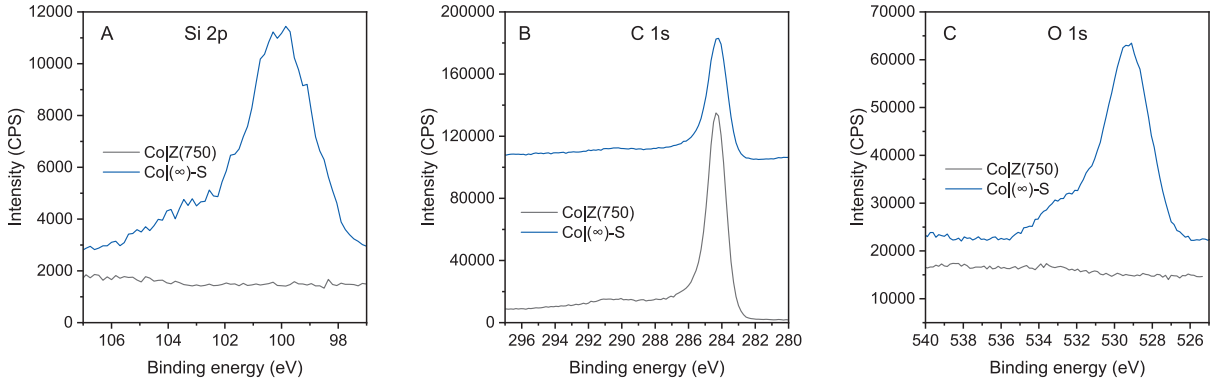

Fig. 11. XPS spectra of Si 2p (A), C 1s (B), and O 1s (C) core levels of the Co|Z(750) (black line) and Co|Z(∞)-S (blue line) catalysts after 160 h in the ESR process conditions (500 °C, EtOH:H_2O = 1:12). (For interpretation of the references to colour in this figure legend, the reader is referred to the web version of this article.). (For interpretation of the references to color in this figure legend, the reader is referred to the web version of this article.)

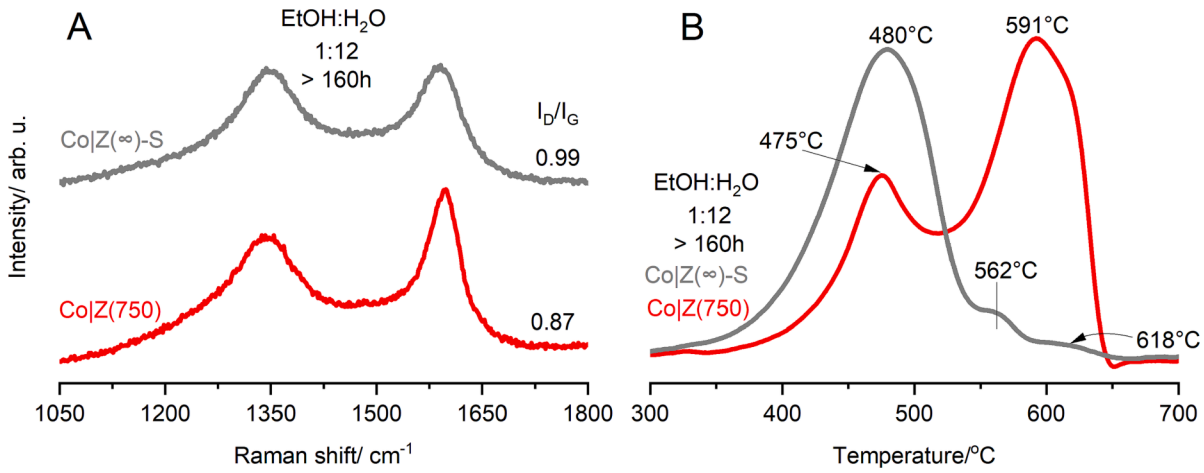

Fig. 12. Raman spectra (A), and weight loss ratio profiles from thermogravimetric studies (B), over Co|Z(750) and Co|Z(∞)-S catalysts after 160 h in the ESR process conditions (500 °C, EtOH:H_2O = 1:12).

catalysts. The comparison of the values of the determined I_D/I_G indicates a greater homogeneity of the deposit formed on it over Co|Z(∞)-S catalyst. The mass loss profiles for Co|Z(750) and Co|Z(∞)-S indicates also the differentiated extent of carbon deposit formation and its various nature (Fig. 12B). A substantially higher share of the low-temperature peak (480 °C) and lower light-off temperature for Co|Z(∞)-S in the weight loss ratio profiles confirm distinct coke deposit combustion processes for the two ESR catalysts. This difference can be explained by the better dispersion of the cobalt phase in Co|Z(∞)-S catalyst, which acts as a soot combustion catalyst in this case, and the presence of the share of coke characterized by higher degree of graphitization, which burns off at higher temperatures.

4. Conclusions

The results presented in this work pointed out a key role of the zeolite support acidity and morphology and indicated that their adjustment allows us to get the ESR catalyst with extraordinary catalytic parameters (100% conversion of ethanol, >90% selectivity to H_2, high stability at 500 °C and EtOH:H_2O 1:12). They overthrow the existing paradigm of low activity and stability of zeolite-based ESR catalysts, opening the way to the development of competitive catalysts with a high application potential. To develop novel ESR catalysts based on the zeolitic supports new synthesis protocols should be optimized to obtain their pure silica versions.

To understand the enhancement in ESR activity with the decrease in the Al content in zeolite framework, the catalysts acidity (FT-IR spectroscopic studies of pyridine and CO sorption studies), reducibility (H_2-TPR), redox properties (*in situ* XPS), and morphology (HR-TEM) were studied. It was found that the decrease in selectivity to the undesired C_2H_4 product with the decrease in the Al content strongly correlates with the acidity of the zeolite support and its impact on the oxidation state of the cobalt phase.

The high selectivity and stability of the cobalt catalysts based on high-silica (Z(750) and pure silica nanometric (Z(∞)-S) zeolite supports correspond to a relatively low degree of carbon deposit formation over the catalysts, confirmed by their extensive *post mortem* characterization (TGA, HR-TEM). The relatively low carbon deposit formation was also inferred from the in-depth insight into the reaction mechanism with *operando* spectroscopic ESR studies (UV–Vis, FT-IR). We attributed the strong advantage of nanometric zeolite support to the highest reducibility and dispersion of the cobalt phase.

Author Contributions

GG: Conceptualization, Methodology, Investigation (RS, TGA), Formal analysis, Resources, Writing – original draft, Writing – review & editing, Supervision, Project administration, Funding acquisition. **MG**: Investigation (catalytic tests), Formal analysis, Data curation. **PP**: Investigation, (catalysts synthesis, RS), Formal analysis **PS**: Formal analysis (XPS), Data curation, Writing – review & editing. **KT:** Investigation (zeolite supports synthesis, *operando* UV–Vis and FTIR), Writing – review & editing **GS**: Investigation (TEM/EDX and FFT), Formal analysis, Data curation, **MR**: Investigation (H_2-TPR), Formal analysis.

SV and FR: Methodology (zeolite synthesis), Writing – review & editing, **KGM**: Methodology (UV–Vis, FT-IR), Formal analysis, Writing – review & editing.

All authors have read and agreed to the published version of the manuscript.

Declaration of Competing Interest

The authors declare that they have no known competing financial interests or personal relationships that could have appeared to influence the work reported in this paper.

Data availability

Data will be made available on request.

Acknowledgments

The work was financed by Grant No. 2021/43/D/ST4/03016 from the National Science Centre, Poland.

K.T. and K.G.M. acknowledge the financial support from National Science Centre of Poland (grant 2020/37/B/ST4/01215).

The open-access publication of this article has been supported by a grant from the Faculty of Chemistry under the Strategic Programme Excellence Initiative at Jagiellonian University.

Appendix A. Supplementary data

Supplementary data to this article can be found online at https://doi.org/10.1016/j.cej.2023.143239.

References

[1] M. Sinaei Nobandegani, L. Yu, J. Hedlund, Zeolite membrane process for industrial CO_2/CH_4 separation, Chem. Eng. J. 446 (2022), 137223, https://doi.org/10.1016/j.cej.2022.137223.

[2] J. Shan, Z. Li, Z. Chen, D. Wang, X. Zhang, Z. Ning, Y. Xue, S. Zhu, Enhancement in catalytic performance of HZSM-5 zeolite for glycerol dehydration after acidity regulation, Chem. Eng. J. 460 (2023), 141741, https://doi.org/10.1016/j.cej.2023.141741.

[3] N.R. Demikhova, M.I. Rubtsova, G.A. Kireev, K.A. Cherednichenko, V. A. Vinokurov, A.P. Glotov, Micro-mesoporous catalysts based on ZSM-5 zeolite synthesized from natural clay nanotubes: Preparation and application in the isomerization of C-8 aromatic fraction, Chem. Eng. J. 453 (2023), 139581, https://doi.org/10.1016/j.cej.2022.139581.

[4] A. Wang, M. Elena Azzoni, J. Han, K. Xie, L. Olsson, Insight into the effect of phosphorus poisoning of Cu/zeolites with different framework towards NH_3-SCR, Chem. Eng. J. 454 (2023), 140040, https://doi.org/10.1016/j.cej.2022.140040.

[5] B.M. Weckhuysen, J. Yu, Recent advances in zeolite chemistry and catalysis, Chem. Soc. Rev. 44 (2015) 7022–7024, https://doi.org/10.1039/c5cs90100f.

[6] Y. Li, L. Li, J. Yu, Applications of zeolites in sustainable chemistry, Chem. 3 (2017) 928–949, https://doi.org/10.1016/j.chempr.2017.10.009.

[7] A. Chica, Zeolites: Promised materials for the sustainable production of hydrogen, ISRN Chem. Eng. 2013 (2013) 1–19, https://doi.org/10.1155/2013/907425.

[8] G. Grzybek, M. Greluk, K. Tarach, K. Pyra, G. Słowik, M. Rotko, K. Góra-Marek, Bioethanol steam reforming over cobalt-containing USY and ZSM-5 commercial zeolite catalysts, Front. Mater. 7 (2020), 597528, https://doi.org/10.3389/fmats.2020.597528.

[9] B.S. Kwak, J.S. Lee, J.S. Lee, B.H. Choi, M.J. Ji, M. Kang, Hydrogen-rich gas production from ethanol steam reforming over Ni/Ga/Mg/Zeolite Y catalysts at mild temperature, Appl. Energy. 88 (2011) 4366–4375, https://doi.org/10.1016/j.apenergy.2011.05.017.

[10] G. Grzybek, K. Góra-Marek, K. Tarach, K. Pyra, P. Patulski, M. Greluk, G. Słowik, M. Rotko, A. Kotarba, Tuning the properties of the cobalt-zeolite nanocomposite catalyst by potassium: switching between dehydration and dehydrogenation of ethanol, J. Catal. 407 (2022) 364–380, https://doi.org/10.1016/j.jcat.2022.02.006.

[11] J.F. da Costa-Serra, M.T. Navarro, F. Rey, A. Chica, Sustainable production of hydrogen by steam reforming of ethanol using cobalt supported on nanoporous zeolitic material, Nanomaterials 10 (2020) 1–13, https://doi.org/10.3390/nano10101934.

[12] F.C. Campos-Skrobot, R.C.P. Rizzo-Domingues, N.R.C. Fernandes-Machado, M. P. Cantão, Novel zeolite-supported rhodium catalysts for ethanol steam reforming, J. Power Sources. 183 (2008) 713–716, https://doi.org/10.1016/j.jpowsour.2008.05.066.

[13] S. Wang, B.o. He, R. Tian, X.u. Wu, X. An, Y. Liu, J. Su, Z. Yu, X. Xie, Novel core-shell-like Ni-supported hierarchical beta zeolite catalysts on bioethanol steam reforming, Fuel 45 (33) (2020) 16409–16420.

[14] X. Li, Z. Zheng, S. Wang, C. Sun, R. Dai, X. Wu, X. An, X. Xie, Preparation and characterization of core-shell composite zeolite BEA@MFI and their catalytic properties in ESR, Catal. Lett. 149 (2019) 766–777, https://doi.org/10.1007/s10562-018-2638-3.

[15] S. Wang, B. He, R. Tian, C. Sun, R. Dai, X. Li, X. Wu, X. An, X. Xie, Ni-hierarchical Beta zeolite catalysts were applied to ethanol steam reforming: Effect of sol gel method on loading Ni and the role of hierarchical structure, Mol. Catal. 453 (2018) 64–73, https://doi.org/10.1016/j.mcat.2018.04.034.

[16] Z. Zheng, C. Sun, R. Dai, S. Wang, X. Wu, X. An, Z. Wu, X. Xie, Ethanol steam reforming on Ni-based catalysts: effect of Cu and Fe addition on the catalytic activity and resistance to deactivation, Energy Fuels 31 (2017) 3091–3100, https://doi.org/10.1021/acs.energyfuels.6b03016.

[17] W. Gac, M. Greluk, G. Słowik, Y. Millot, L. Valentin, S. Dzwigaj, Effects of dealumination on the performance of Ni-containing BEA catalysts in bioethanol steam reforming, Appl. Catal. B Environ. 237 (2018) 94–109, https://doi.org/10.1016/j.apcatb.2018.05.040.

[18] J.F. Da Costa-Serra, M.T. Navarro, F. Rey, A. Chica, Bioethanol steam reforming on Ni-based modified mordenite. Effect of mesoporosity, acid sites and alkaline metals, Int. J. Hydrogen Energy 37 (2012) 7101–7108, https://doi.org/10.1016/j.ijhydene.2011.10.086.

[19] A. Chica, S. Sayas, Effective and stable bioethanol steam reforming catalyst based on Ni and Co supported on all-silica delaminated ITQ-2 zeolite, Catal. Today. 146 (2009) 37–43, https://doi.org/10.1016/j.cattod.2008.12.024.

[20] J.F. Da Costa-Serra, A. Chica, Bioethanol steam reforming on Co/ITQ-18 catalyst: Effect of the crystalline structure of the delaminated zeolite ITQ-18, Int. J. Hydrogen Energy. 36 (2011) 3862–3869, https://doi.org/10.1016/J.IJHYDENE.2010.12.094.

[21] L. Lang, S. Zhao, X. Yin, W. Yang, C. Wu, Catalytic activities of K-modified zeolite ZSM-5 supported rhodium catalysts in low-temperature steam reforming of bioethanol, Int. J. Hydrogen Energy 40 (2015) 9924–9934, https://doi.org/10.1016/j.ijhydene.2015.06.016.

[22] A. Kumar, R. Prasad, Y.C. Sharma, Ethanol steam reforming study over ZSM-5 supported cobalt versus nickel catalyst for renewable hydrogen generation, Chinese J. Chem. Eng. 27 (2019) 677–684, https://doi.org/10.1016/j.cjche.2018.03.036.

[23] A.J. Vizcaíno, A. Carrero, J.A. Calles, Hydrogen production by ethanol steam reforming over Cu–Ni supported catalysts, Int. J. Hydrogen Energy 32 (2007) 1450–1461, https://doi.org/10.1016/J.IJHYDENE.2006.10.024.

[24] E.R. López, F. Dorado, A. de Lucas-Consuegra, Electrochemical promotion for hydrogen production via ethanol steam reforming reaction, Appl. Catal. B Environ. 243 (2019) 355–364, https://doi.org/10.1016/j.apcatb.2018.10.062.

[25] V. Palma, F. Castaldo, P. Ciambelli, G. Iaquaniello, CeO_2-supported Pt/Ni catalyst for the renewable and clean H_2 production via ethanol steam reforming, Appl. Catal. B Environ. 145 (2014) 73–84, https://doi.org/10.1016/j.apcatb.2013.01.053.

[26] Z. Xiao, Y. Li, F. Hou, C. Wu, L. Pan, J. Zou, L. Wang, X. Zhang, G. Liu, G. Li, Engineering oxygen vacancies and nickel dispersion on CeO_2 by Pr doping for highly stable ethanol steam reforming, Appl. Catal. B Environ. 258 (2019), 117940, https://doi.org/10.1016/j.apcatb.2019.117940.

[27] T.S. Moraes, R.C. Rabelo Neto, M.C. Ribeiro, L.V. Mattos, M. Kourtelesis, S. Ladas, X. Verykios, F.B. Noronha, Ethanol conversion at low temperature over CeO_2-Supported Ni-based catalysts. Effect of Pt addition to Ni catalyst, Appl. Catal. B Environ. 181 (2016) 754–768, https://doi.org/10.1016/j.apcatb.2015.08.044.

[28] V. Nichele, M. Signoretto, F. Pinna, F. Menegazzo, I. Rossetti, G. Cruciani, G. Cerrato, A. Di Michele, Ni/ZrO_2 catalysts in ethanol steam reforming: Inhibition of coke formation by CaO-doping, Appl. Catal. B Environ. 150–151 (2014) 12–20, https://doi.org/10.1016/j.apcatb.2013.11.037.

[29] M. Kourtelesis, T.S. Moraes, L.V. Mattos, D.K. Niakolas, F.B. Noronha, X. Verykios, The effects of support morphology on the performance of Pt/CeO_2 catalysts for the low temperature steam reforming of ethanol, Appl. Catal. B Environ. 284 (2021) 119757.

[30] L.C. Chen, S.D. Lin, Effects of the pretreatment of $CuNi/SiO_2$ on ethanol steam reforming: Influence of bimetal morphology, Appl. Catal. B Environ. 148–149 (2014) 509–519, https://doi.org/10.1016/j.apcatb.2013.11.031.

[31] J. Sun, A.M. Karim, D. Mei, M. Engelhard, X. Bao, Y. Wang, New insights into reaction mechanisms of ethanol steam reforming on Co-ZrO_2, Appl. Catal. B Environ. 162 (2015) 141–148, https://doi.org/10.1016/j.apcatb.2014.06.043.

[32] Y. Deng, S. Li, L. Appels, H. Zhang, N. Sweygers, J. Baeyens, R. Dewil, Steam reforming of ethanol by non-noble metal catalysts, Renew. Sustain. Energy Rev. 175 (2023), 113184, https://doi.org/10.1016/J.RSER.2023.113184.

[33] R.A. El-Salamony, Catalytic Steam reforming of ethanol to produce hydrogen: modern and efficient catalyst modification strategies, ChemistrySelect 8 (2023), https://doi.org/10.1002/slct.202203195.

[34] Y.C. Sharma, A. Kumar, R. Prasad, S.N. Upadhyay, Ethanol steam reforming for hydrogen production: Latest and effective catalyst modification strategies to minimize carbonaceous deactivation, Renew. Sustain. Energy Rev. 74 (2017) 89–103, https://doi.org/10.1016/j.rser.2017.02.049.

[35] L.V. Mattos, G. Jacobs, B.H. Davis, F.B. Noronha, Production of hydrogen from ethanol: Review of reaction mechanism and catalyst deactivation, Chem. Rev. 112 (2012) 4094–4123, https://doi.org/10.1021/cr2000114.

[36] S. Ogo, Y. Sekine, Recent progress in ethanol steam reforming using non-noble transition metal catalysts: A review, Fuel Process. Technol. 199 (2020), 106238, https://doi.org/10.1016/j.fuproc.2019.106238.

[37] R. Li, C. Liu, L. Li, J. Xu, J. Ma, J. Ni, J. Yan, J. Han, Y. Pan, Y. Liu, L. Lu, Regulating cobalt chemical state by CeO_2 facets preferred exposure for improved ethanol steam reforming, Fuel 336 (2023), 126758, https://doi.org/10.1016/J.FUEL.2022.126758.

[38] J.L. Contreras, J. Salmones, J.A. Colín-Luna, L. Nuño, B. Quintana, I. Córdova, B. Zeifert, C. Tapia, G.A. Fuentes, Catalysts for H_2 production using the ethanol steam reforming (a review), Int. J. Hydrogen Energy 39 (2014) 18835–18853, https://doi.org/10.1016/j.ijhydene.2014.08.072.

[39] H. Inokawa, S. Nishimoto, Y. Kameshima, M. Miyake, Difference in the catalytic activity of transition metals and their cations loaded in zeolite for ethanol steam reforming, Int. J. Hydrogen Energy 35 (2010) 11719–11724, https://doi.org/10.1016/j.ijhydene.2010.08.092.

[40] G. Grzybek, K. Góra-Marek, P. Patulski, M. Greluk, M. Rotko, G. Słowik, A. Kotarba, Optimization of the potassium promotion of the Co|α-Al_2O_3 catalyst for the effective hydrogen production via ethanol steam reforming, Appl. Catal. A Gen. 614 (2021), 118051, https://doi.org/10.1016/j.apcata.2021.118051.

[41] J.L. Guth, H. Kessler, R. Wey, New route to pentasil-type zeolites using a non alkaline medium in the presence of fluoride ions, Kodansha Ltd. (1986), https://doi.org/10.1016/S0167-2991(09)60864-8.

[42] T. Marqueno, D. Santamaria-Perez, J. Ruiz-Fuertes, R. Chuliá-Jordán, J.L. Jordá, F. Rey, C. McGuire, A. Kavner, S. Macleod, D. Daisenberger, C. Popescu, P. Rodriguez-Hernandez, A. Munoz, An ultrahigh CO_2-loaded silicalite-1 zeolite: Structural stability and physical properties at high pressures and temperatures, Inorg. Chem. 57 (2018) 6447–6455, https://doi.org/10.1021/acs.inorgchem.8b00523.

[43] K. Góra-Marek, B. Gil, J. Datka, Quantitative IR studies of the concentration of Co^{2+} and Co^{3+} sites in zeolites CoZSM-5 and CoFER, Appl. Catal. A Gen. 353 (2009) 117–122, https://doi.org/10.1016/j.apcata.2008.10.034.

[44] G. Słowik, M. Greluk, M. Rotko, A. Machocki, Evolution of the structure of unpromoted and potassium-promoted ceria-supported nickel catalysts in the steam reforming of ethanol, Appl. Catal. B Environ. 221 (2018) 490–509, https://doi.org/10.1016/j.apcatb.2017.09.052.

[45] N. Fairley, V. Fernandez, M. Richard-Plouet, C. Guillot-Deudon, J. Walton, E. Smith, D. Flahaut, M. Greiner, M. Biesinger, S. Tougaard, D. Morgan, J. Baltrusaitis, Systematic and collaborative approach to problem solving using X-ray photoelectron spectroscopy, Appl. Surf. Sci. Adv. 5 (2021), 100112, https://doi.org/10.1016/j.apsadv.2021.100112.

[46] M.C. Biesinger, B.P. Payne, A.P. Grosvenor, L.W.M. Lau, A.R. Gerson, R.S.C. Smart, Resolving surface chemical states in XPS analysis of first row transition metals, oxides and hydroxides: Cr, Mn, Fe, Co and Ni, Appl. Surf. Sci. 257 (2011) 2717–2730, https://doi.org/10.1016/j.apsusc.2010.10.051.

[47] G. Grzybek, M. Greluk, P. Indyka, K. Góra-Marek, P. Legutko, G. Słowik, S. Turczyniak-Surdacka, M. Rotko, Z. Sojka, A. Kotarba, Cobalt catalyst for steam reforming of ethanol–Insights into the promotional role of potassium, Int. J. Hydrogen Energy 5 (2020) 22658–22673, https://doi.org/10.1016/j.ijhydene.2020.06.037.

[48] K.I. Hadjiivanov, G.N. Vayssilov, Characterization of oxide surfaces and zeolites by carbon monoxide as an IR probe molecule, Adv. Catal. 47 (2002) 307–511, https://doi.org/10.1016/S0360-0564(02)47008-3.

[49] J. Ansorge, H. Förster, Transient IR spectroscopic investigation of surface-carbonyl formation on a supported cobalt catalyst, J. Catal. 68 (1981) 182–185, https://doi.org/10.1016/0021-9517(81)90051-8.

[50] D.C. Koningsberger, J. De Graaf, B.L. Mojet, D.E. Ramaker, J.T. Miller, The metal-support interaction in Pt/Y zeolite: Evidence for a shift in energy of metal d-valence orbitals by Pt-H shape resonance and atomic XAFS spectroscopy, Appl. Catal. A Gen. 191 (2000) 205–220, https://doi.org/10.1016/S0926-860X(99)00320-8.

[51] K.A. Tarach, A. Śrębowata, E. Kowalewski, K. Gołąbek, A. Kostuch, K. Kruczała, V. Girman, K. Góra-Marek, Nickel loaded zeolites FAU and MFI: Characterization and activity in water-phase hydrodehalogenation of TCE, Appl. Catal. A Gen. 568 (2018) 64–75, https://doi.org/10.1016/j.apcata.2018.09.026.

[52] G. Grzybek, K. Ciura, S. Wójcik, J. Gryboś, P. Indyka, M. Inger, K. Antoniak-Jurak, P. Kowalik, A. Kotarba, Z. Sojka, On the selection of the best polymorph of Al_2O_3 carriers for supported cobalt nano-spinel catalysts for N_2O abatement: An interplay between preferable surface spreading and damaging active phase-support interaction, Catal. Sci. Technol. 7 (2017) 5723–5732, https://doi.org/10.1039/c7cy01575e.

[53] R. Bhargava, S. Khan, N. Ahmad, M.M.N. Ansari, Investigation of structural, optical and electrical properties of Co_3O_4 nanoparticles, AIP Conf. Proc. 1953 (2018) 1–5, https://doi.org/10.1063/1.5032369.

[54] I. Kiricsi, H. Förster, G. Tasi, J.B. Nagy, Generation, characterization, and transformations of unsaturated carbenium ions in zeolites, Chem. Rev. 99 (1999) 2085–2114, https://doi.org/10.1021/cr9600767.

[55] M. Bjørgen, F. Bonino, S. Kolboe, K.P. Lillerud, A. Zecchina, S. Bordiga, Spectroscopic evidence for a persistent benzenium cation in zeolite H-beta, J. Am. Chem. Soc. 125 (2003) 15863–15868, https://doi.org/10.1021/ja037073d.

[56] J. Melsheimer, D. Ziegler, Ethene transformation on HZSM-5 studied by combined UV-VIS spectroscopy and on-line gas chromatography, J. Chem. Soc. Faraday Trans. 88 (1992) 2101–2210, https://doi.org/10.1039/FT9928802101.

[57] M. Hunger, W. Wang, Formation of cyclic compounds and carbenium ions by conversion of methanol on weakly dealuminated zeolite H-ZSM-5 investigated via a novel in situ CF MAS NMR/UV-Vis technique, Chem. Commun. 4 (2004) 584–585, https://doi.org/10.1039/b315779b.

[58] E. Kukulska-Zajac, K. Gora-Marek, J. Datka, IR and TPD studies of the reaction of acetic acid in zeolites NaHY, Microporous Mesoporous Mater. 96 (2006) 216–221, https://doi.org/10.1016/j.micromeso.2006.06.03.

[59] F.J. Valencia, J. Santiago, R.I. González, R. González-Arrabal, C. Ruestes, M. Perez Díaz, M.A. Monclus, J. Molina-Aldareguia, P.D. Nuñez, F. Munoz, M. Kiwi, J. M. Perlado, E.M. Bringa, Nanoindentation of Amorphous Carbon: a combined experimental and simulation approach, Acta Mater. 203 (2021), 116485, https://doi.org/10.1016/j.actamat.2020.116485.